Establishing synthetic ribbon-type active zones in a heterologous expression system

Rohan Kapoor[1,2,3], Niko Schwenzer[4,5,7], Thomas Dresbach[6], Stephan E. Lehnart[4,5,7] & Tobias Moser[1,2,7]

[1]Institute for Auditory Neuroscience and InnerEarLab, University Medical Center Göttingen, Germany.

[2]Auditory Neuroscience and Synaptic Nanophysiology Group, Max-Planck-Institute for Multidisciplinary Sciences, Göttingen, Germany.

[3]IMPRS Molecular Biology, Göttingen Graduate School for Neuroscience and Molecular Biosciences, University of Göttingen, Göttingen, Germany

[4]Department of Cardiology and Pneumology, University Medical Center Göttingen; Göttingen, Germany.

[5]Cellular Biophysics & Translational Cardiology Section, Heart Research Center Göttingen, University Medical Center Göttingen, Germany.

[6]Institute of Anatomy and Embryology, University Medical Center Göttingen; Göttingen, Germany.

[7]Cluster of Excellence "Multiscale Bioimaging: from Molecular Machines to Networks of Excitable Cells" (MBExC 2067), University of Göttingen, Germany

Correspondence: tmoser@gwdg.de

Character count: 70,263

Abstract

Encoding of several sensory modalities into neural signals is mediated by ribbon synapses. The synaptic ribbon tethers synaptic vesicles at the presynaptic active zone (AZ) and might act as a super-scaffold organizing AZ topography. Here we employed a synthetic biology approach to reconstitute ribbon-type AZs in HEK293 cells for probing their minimal molecular requirements and studying presynaptic Ca^{2+} channel clustering. Co-expressing a membrane-targeted version of the AZ-protein Bassoon and the ribbon core protein RIBEYE, we observed structures recapitulating basic aspects of ribbon-type AZs, which we call *synthetic* ribbons or *SyRibbons*. *SyRibbons* with Ca^{2+} channel clusters formed upon additional expression of $Ca_V1.3$ Ca^{2+} channels and RIM-binding protein 2 (RBP2), known to promote presynaptic Ca^{2+} channel clustering. Confocal and super-resolution microscopy along with functional analysis by patch-clamp and Ca^{2+}-imaging revealed striking similarities and interesting differences of *SyRibbons* in comparison to native IHC ribbon-type AZs. In summary, we identify Ca^{2+} channels, RBP, membrane-anchored Bassoon, and RIBEYE as minimal components for reconstituting a basic ribbon-type AZ. *SyRibbons* might complement animal studies on molecular interactions of AZ proteins.

Keywords: calcium channel/channel cluster/calcium signal/ribbon synapse/synthetic biology

Significance Statement

Encoding of sensory information in our eyes and ears builds on specialized ribbon synapses of sensory cells. Elucidating the molecular underpinning of their fascinating structure and function is an ongoing effort to which we add a bottom-up reconstitution approach in cultured cells. Aiming to recapitulate basic properties of ribbon-type presynaptic active zones of cochlear inner hair cells, we identified a minimal set of proteins that assemble in cellular nanodomains, structurally and functionally alike active zones. While not yet reconstituting synaptic vesicle exocytosis, we consider the established synthetic ribbon-type active zones a valuable platform for studying molecular interactions of active zone proteins. We expect the approach to complement, refine, and reduce experiments on native ribbon synapses asserted from animals.

Introduction

Synapses of sensory receptor cells of the inner ear and the retina are hallmarked by the presence of an electron-dense structure called the synaptic ribbon, which tethers synaptic vesicles (SVs) at the presynaptic active zone (AZ, [Moser *et al*, 2019; Matthews & Fuchs, 2010]). Proposed functional roles of the ribbon include (i) its role as a SV replenishment machine for tireless neurotransmission (Bunt, 1971; Holt *et al*, 2004; Khimich *et al*, 2005; Frank *et al*, 2010; Snellman *et al*, 2011; Graydon *et al*, 2011;

56 Vaithianathan *et al*, 2016), (ii) "super-scaffold" regulating the abundance, topography, and function of
57 AZ players such Ca^{2+} channels and release sites and their tight coupling (Khimich *et al*, 2005; Frank *et*
58 *al*, 2010; Wong *et al*, 2014; Maxeiner *et al*, 2016; Jean *et al*, 2018; Grabner & Moser, 2021), and iii)
59 coordination of SV release (Heidelberger *et al*, 1994; Glowatzki & Fuchs, 2002; Singer *et al*, 2004;
60 Edmonds, 2004; Mehta *et al*, 2013). Yet, our molecular understanding of how these postulated
61 functions are executed by synaptic ribbons is still limited.

62 Likewise, the clustering of Ca^{2+} channels at the AZ, how it is varied among different or even the
63 same synapse types and how the ribbon contributes towards this, remain active areas of research. For
64 example, ribbon synapses of mature inner hair cells (IHC) assemble $Ca_V1.3$ voltage-gated Ca^{2+} channels
65 at the base of the ribbon, but vary in shape, size and channel complement (20-330) of the $Ca_V1.3$
66 clusters (Frank *et al*, 2010; Wong *et al*, 2014; Neef *et al*, 2018) partially dependent on the position
67 within the IHC (Ohn *et al*, 2016; Özçete & Moser, 2021). IHC synapses lacking AZ-anchored ribbons in
68 Bassoon mutant mice showed fewer Ca^{2+} channels with altered topography (Frank *et al*, 2010; Neef *et*
69 *al*, 2018). While genetic disruption of Ca^{2+} channel-tethering AZ proteins RIM2 (Jung *et al*, 2015) and
70 RBP2 (Krinner *et al*, 2017) reduced the abundance of Ca^{2+} channels at IHC synapses, their topography
71 retained the typical stripe-like shape of Ca^{2+} clusters. Constitutive deletion of RIBEYE, the core scaffold
72 protein of the synaptic ribbon, provided, so far, the most direct test of the scaffolding role of the ribbon
73 (Maxeiner *et al*, 2016; Jean *et al*, 2018; Becker *et al*, 2018; Grabner & Moser, 2021). Here, ribbon-less
74 synapses of IHCs showed an altered Ca^{2+} channel topography with a more spatially widespread
75 presynaptic Ca^{2+} signal but intact Ca^{2+} channel complement (Jean *et al*, 2018). Moreover, the voltage-
76 dependence of activation as well as the inactivation of Ca^{2+} channels appeared to be altered,
77 suggesting a possible role of the synaptic ribbon in also regulating Ca^{2+} channel physiology (Jean *et al*,
78 2018). Changes in Ca^{2+} channel physiology upon deletion of RIBEYE were also found for $Ca_V1.4$ at
79 ribbon-less rod photoreceptor AZs (Grabner & Moser, 2021). Finally, IHCs lacking piccolino, a ribbon-
80 synapse specific isoform of the AZ protein piccolo, show AZs with smaller synaptic ribbons and altered
81 clustering yet normal complement of Ca^{2+} channels (Michanski *et al*, 2023).

82 So how does the synaptic ribbon tune into the orchestra of AZ proteins that collectively
83 organize Ca^{2+} channel abundance, topography, and function? To what extent can the effects observed
84 upon disruption of Bassoon be attributed to the concomitant loss of the ribbon? These questions seem
85 even more relevant given that, so far to our knowledge, no direct interactions between Bassoon (Frank
86 *et al*, 2010) or RIBEYE and the Ca^{2+} channel have been described. Here, we adopted a bottom-up
87 synthetic biology approach to assemble a minimal presynaptic protein machinery required to bring
88 together RIBEYE and Ca^{2+} channels in a heterologous expression system to assess the role of the
89 synaptic ribbon in regulating Ca^{2+} channel clustering and physiology. Similar approaches have
90 previously been employed for reconstituting aspects of conventional synapses, for instance in "hemi-

synapses" between co-cultured neurons and non-neuronal cells overexpressing presynaptic or postsynaptic components (for review see Craig *et al*, 2006). More recently, Munc13-1 supra-molecular assemblies which recruit release machinery proteins were reconstituted (Sakamoto *et al*, 2018).

Expression of RIBEYE in synapse-naïve cell lines such as COS-7 cells led to large cytosolic assemblies (Schmitz *et al*, 2000). Membrane-proximal RIBEYE clusters and ribbon-like electron dense structures with vesicles could be found in a retinal progenitor cell-line (R28, [Magupalli *et al*, 2008]) yet, these cells might not be considered synapse-naïve. Regardless, the presence and function of Ca^{2+} channels at synthetic ribbon synapses have not yet been studied. The need for co-expressing at least three Ca^{2+} channel subunits ($Ca_V\alpha_x$, $Ca_V\beta_x$ and $Ca_V\alpha_2\delta_x$) in synapse-naïve cell lines renders acute co-expression of AZ multidomain proteins cumbersome. Here we took advantage of synapse-naïve Human Embryonic Kidney 293 (HEK293) cells stably expressing inducible $Ca_V1.3\alpha_1$, which is the predominant subtype of voltage-gated Ca^{2+} channels at IHC ribbon synapses (Brandt *et al*, 2003; Platzer *et al*, 2000; Dou *et al*, 2004), as well as constitutively expressed $Ca_V\beta_3$ and $Ca_V\alpha_2\delta_1$. We co-expressed RIBEYE along with membrane targeted Bassoon and observed structures with striking resemblance to IHC synaptic ribbon-type AZs. We characterized the structure and function of these synthetic ribbon-type AZs and identified Bassoon, RBP2, RIBEYE and $Ca_V1.3$ channels as the minimal components required for assembling a basic ribbon-type AZ. We observed that synthetic ribbons recruit $Ca_V1.3$ channels in large clusters and show localized Ca^{2+} influx upon stimulation. Our results support the role of synaptic ribbons in promoting $Ca_V1.3$ channel clustering. Synthetic ribbon-type AZs offer a novel approach for functionally studying protein-protein interaction and will likely complement, refine and reduce experiments on native ribbon synapses.

Results

Membrane-targeted Bassoon recruits RIBEYE to the cell membrane in HEK293 cells where structures alike inner hair cell synaptic ribbons are formed.

Human epithelial HEK293 cells have the advantage of not expressing the synaptic machinery components studied here. This provides a clean background for reconstituting synthetic synapses from a minimal set of synaptic proteins. Our first step towards assembling a ribbon-type AZ in a heterologous expression system was to express RIBEYE, the core scaffold protein of the synaptic ribbon, and target it to the cell membrane. We performed transient transfection of a RIBEYE construct with a C-terminal EGFP tag in HEK293 cells and observed large spherical clusters of RIBEYE that appeared largely cytosolic (Fig 1Aii), in contrast to a diffuse cytosolic distribution when merely expressing EGFP (Fig 1Ai). These RIBEYE clusters form due to self-assembling properties of RIBEYE via multiple sites of homophilic interaction as have been demonstrated before in several cell lines. They do not colocalize with the endoplasmic reticulum (ER), Golgi apparatus, or lysosomes and hence, are

126 unlikely to reflect RIBEYE entrapped in protein trafficking pathways or to represent degradation
127 products of overexpressed RIBEYE (Fig EV1 A, B and C).

128 Next, for membrane targeting of these cytosolic RIBEYE clusters, we co-expressed Bassoon (Fig 1Aiii).
129 Prior work on the molecular underpinnings of ribbon synapses had identified the multidomain
130 cytomatrix of the active zone protein Bassoon (tom Dieck *et al*, 1998) to critically contribute to
131 anchoring the synaptic ribbon to the AZ membrane (Khimich *et al*, 2005; Dick *et al*, 2003; tom Dieck *et*
132 *al*, 2005). Co-expression of full-length Bassoon along with RIBEYE in HEK293 cells showed colocalizing
133 clusters of the two proteins that, however, remained largely cytosolic (Fig 1Aiv).

134 Next, for plasma membrane-targeting of Bassoon, we generated a construct by removing the first 95
135 N-terminal amino acids of Bassoon and replacing these with a palmitoylation consensus sequence of
136 the neuronal Growth Associated Protein 43 (GAP43). We refer to this as palm-Bassoon throughout,
137 and we used constructs with and without a C-terminal EGFP tag (Fig 1B). Expression of either of these
138 palm-Bassoon constructs in HEK293 cells showed comparable immunofluorescence patterns with
139 Bassoon puncta spread across the periphery of the cell, largely colocalizing with the endogenously
140 expressed membrane protein Na, K-ATPase α_1 (data representative of 3 transfections, Fig 1C, D).
141 Comparing the ratio of Bassoon signal intensity at the periphery *versus* inside of the cell in randomly
142 selected single sections from confocal stacks of palm-Bassoon and Bassoon transfected cells (N = 10
143 cells, 3 transfections per group, Fig 1E) demonstrated a higher Bassoon signal intensity at the periphery
144 of cells expressing the palm-Bassoon construct (****P < 0.0001, Mann-Whitney-Wilcoxon test),
145 implying successful plasma membrane targeting of Bassoon.

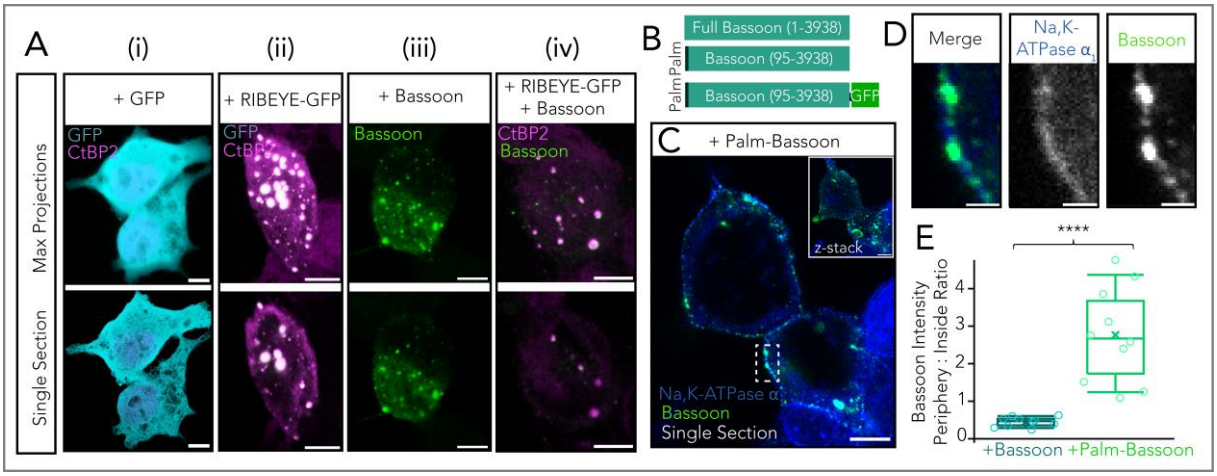

146

147 **Figure 1 - Membrane targeting of Bassoon using a palmitoylation consensus sequence.**

148 **A** Representative confocal images of HEK293 cells transfected with (i) GFP only (CtBP2/RIBEYE in
149 magenta labeling nuclei, GFP in cyan), (ii) RIBEYE-GFP (CtBP2/RIBEYE in magenta, GFP in cyan), (iii)
150 Bassoon (green) and (iv) RIBEYE-GFP and Bassoon. Note that antibodies against RIBEYE B-domain
151 and the nuclear transcription factor CtBP2 result in similar staining patterns as CtBP2 is transcribed
152 from the same gene as RIBEYE and is identical to the RIBEYE-B domain except for the first 20 N-

153 terminal amino acids. Upper panel shows maximum projections and lower panel shows exemplary
154 single sections from confocal stacks. Scale bar = 5 µm.

155 **B** Schematic of construct for membrane targeting of Bassoon. The first 95 amino acids from full-
156 length Bassoon were replaced with a palmitoylation consensus sequence from GAP43. Constructs
157 without and with a C-terminal GFP tag were used, as depicted.

158 **C** Sample confocal image (single section) showing membrane targeted palm-Bassoon (green)
159 expressed in HEK293 cells appears as puncta distributed along the periphery of the cell, marked
160 by Na, K-ATPase α_1(blue). Inset shows maximal projection of confocal section. Scale bar = 5µm.

161 **D** Zoom-in from **(C)** shows colocalisation of palm-Bassoon with membrane marker Na, K-ATPase α1.
162 Scale bar = 1µm.

163 **E** Quantification of Bassoon signal intensity at periphery *vs* inside of cell. Cells expressing palm-
164 Bassoon (N = 10 cells) clearly show a higher peripheral distribution compared to cells expressing
165 full-length Bassoon (N = 10 cells), ****P < 0.0001, Mann-Whitney-Wilcoxon test. Overlaid data
166 points represent individual cells, crosses represent the mean values, central band indicates the
167 median, whiskers represent 90/10 percentiles, and boxes represent 75/25 percentiles.

168

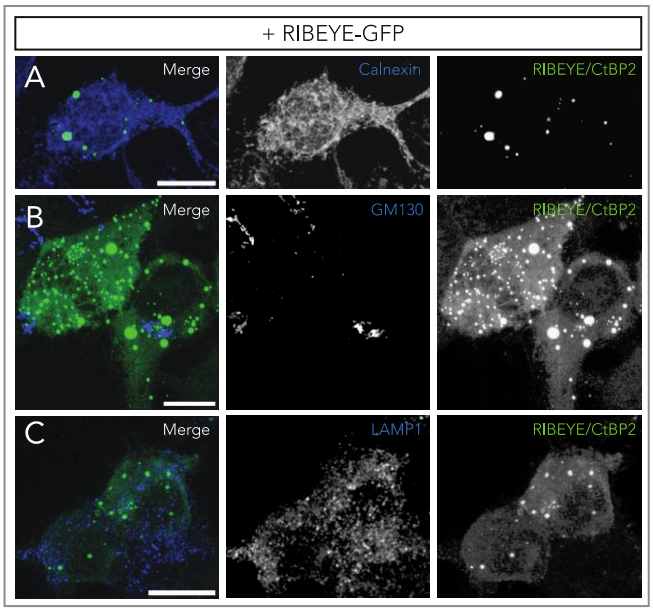

169

170 **Figure EV1 - Subcellular distribution of RIBEYE clusters in HEK293 cells.**
171 Maximal projections of confocal sections of HEK293 cells transfected with RIBEYE-GFP (green).
172 Representative co-staining for **(A)** calnexin (endoplasmic reticulum marker), **(B)** GM130 (cis-Golgi
173 marker) and **(C)** LAMP1 (lysosomal marker) have been shown respectively (blue). RIBEYE clusters do
174 not appear to localize in either of the three compartments. Scale bar = 10 µm.

175

176 Next, we co-expressed palm-Bassoon and RIBEYE in HEK293 cells and observed colocalizing RIBEYE and
177 Bassoon immunofluorescent puncta at the periphery of cells (7 transfections; Fig 2Ai). Closer
178 inspection of these immunofluorescent puncta with STimulated Emission Depletion (STED) nanoscopy
179 (Fig 2Aii) revealed discrete structures typically consisting of ellipsoidal RIBEYE clusters juxtaposing on
180 top of plate-like palm-Bassoon structures which seemingly anchor the RIBEYE clusters to the plasma
181 membrane. Interestingly, we found the morphology of the RIBEYE + palm-Bassoon structures to be

182 strikingly reminiscent of the arrangement of the two proteins in IHC ribbon synapses, where an
183 ellipsoid/spherical synaptic ribbon composed of RIBEYE is found seated on a Bassoon plate that
184 anchors it to the presynaptic AZ membrane (e.g. Wong *et al*, 2014; Michanski *et al*, 2019, 2023) (Fig
185 2B, i and ii; data from Michanski *et al*, 2023).

186 We compared the RIBEYE and Bassoon signal intensities at the periphery *versus* inside of the
187 cell in randomly selected single sections from confocal stacks of HEK cells expressing RIBEYE and palm-
188 Bassoon (N = 9 cells) and HEK cells expressing RIBEYE and full-length Bassoon (N=9 cells). We found an
189 increased peripheral distribution of both RIBEYE and Bassoon when using palm-Bassoon (Fig 2C, ****P
190 < 0.0001, Mann-Whitney-Wilcoxon test), implying successful membrane targeting of RIBEYE by palm-
191 Bassoon. In each transfection, ~10% cells showed co-expression of both RIBEYE and palm-Bassoon (for
192 representative sample overview see Fig EV2). Of those, cells expressing discrete RIBEYE-palm Bassoon
193 structures were discernible by the characteristic RIBEYE distribution along the periphery of the cell.
194 This peripheral distribution in turn seemingly depends upon RIBEYE and palm-Bassoon expression
195 ratios (shown in Figure EV2B) as cells with little to no palm-Bassoon expression show predominantly
196 cytosolic RIBEYE puncta and were not used for analysis. For simplicity, we henceforth refer to the
197 structures composed of RIBEYE and palm-Bassoon in HEK293 cells as *SyRibbons* (for *synthetic* ribbons).

198 We next performed three-dimensional surface renderings using *Imaris* 9.6 (Oxford
199 Instruments) to assess these structures. In a given cell, only structures with colocalizing RIBEYE and
200 palm-Bassoon immunofluorescence were considered for analysis to exclude the occasional non-
201 membrane localized spots (on average 51.75 ± 40.84 RIBEYE surfaces colocalizing with Bassoon
202 surfaces per cell; N = 20 cells). The volumes of RIBEYE and palm-Bassoon surfaces of *SyRibbons* were
203 smaller on average and more variable (average volume ± standard deviation (SD) = 0.19 ± 0.23 μm^3
204 with a coefficient of variation (CV) = 1.23 for RIBEYE; n_{spots} = 864 and volume = 0.17 ± 0.18 μm^3 with CV
205 = 1.10 for Bassoon; n_{spots} = 951; data from N = 20 cells, quantifications from 5 sample transfections)
206 than volumes of synaptic ribbons and Bassoon immunofluorescent puncta from rat IHCs (volume =
207 0.29 ± 0.17 μm^3, CV = 0.59 for RIBEYE; n_{spots} = 290, and volume = 0.27 ± 0.18 μm^3, CV = 0.67 for Bassoon;
208 n_{spots} = 314, data from N = 29 cells), (Figure 2D, E). Moreover, volumes of RIBEYE surfaces show a high
209 positive correlation to volumes of corresponding palm-Bassoon surfaces (P_r = 0.778, ****P < 0.0001),
210 implying larger palm-Bassoon structures may recruit bigger RIBEYE structures to the plasma
211 membrane. We also note that volume of RIBEYE surfaces in *SyRibbons* appears smaller and well-
212 regulated in contrast to the predominantly large, cytosolic RIBEYE assemblies in cells co-expressing
213 RIBEYE and full-length Bassoon (volume = 0.30 ± 0.36 μm^3, n_{spots} = 460, N = 10 cells, ****P < 0.001,
214 Mann-Whitney-Wilcoxon Test). In turn, Bassoon clusters seemed regulated by co-expressed RIBEYE:
215 Bassoon surfaces at the plasma membrane were larger at *SyRibbons* than in the absence of RIBEYE in

cells only expressing palm-Bassoon (volume = 0.14 ± 0.21 µm^3, n_{spots} = 2217, N = 13 cells, ****P < 0.001, Mann-Whitney-Wilcoxon Test).

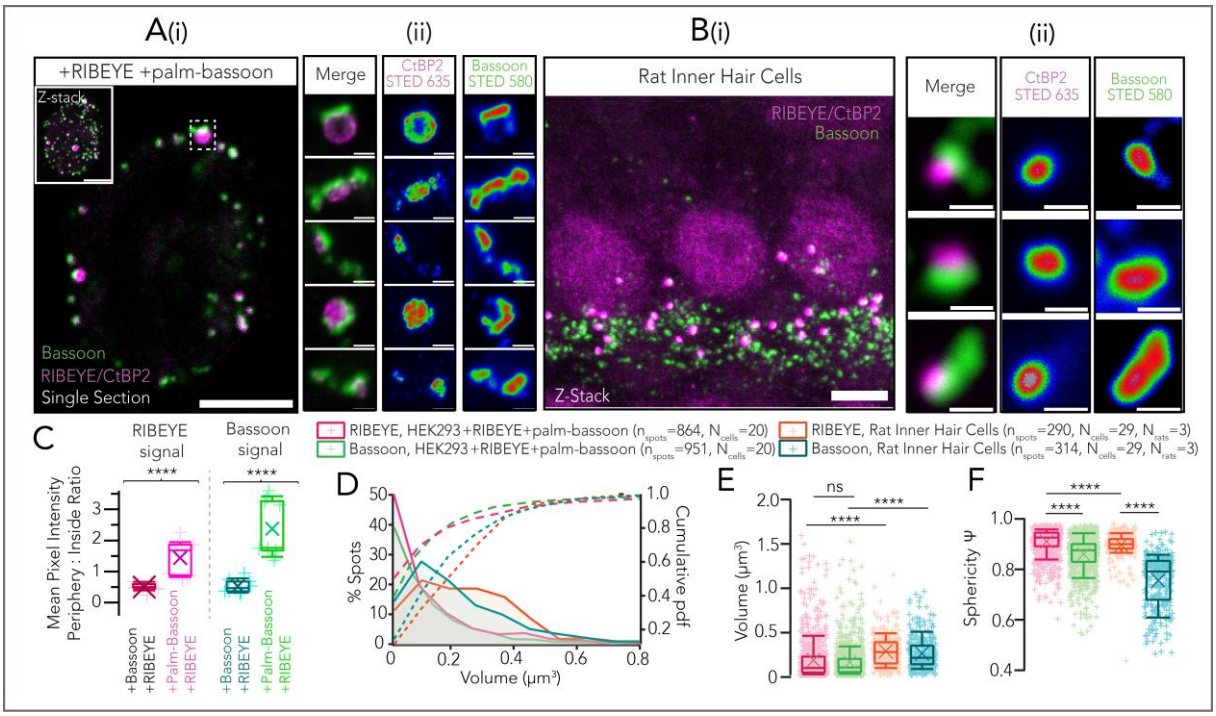

Figure 2 - Co-expression of RIBEYE with palm-Bassoon results in ribbon-type AZ-like structures

A (i) Representative confocal image (single section) of a HEK293 cell transfected with RIBEYE-GFP (magenta) and palm-Bassoon (green). Co-expression of RIBEYE with palm-Bassoon targets RIBEYE to the cell membrane. Inset shows maximum projection. Scale bar = 5µm. (ii) Exemplary 2-D STED images for RIBEYE – palm-Bassoon juxtapositions acquired from cells as shown in (i); Scale bar = 500nm; individual channels have been depicted with an intensity-coded look-up table with warmer colors indicating higher intensity.

B **(i)** Representative maximum projection of confocal sections of apical organ of Corti from a Wistar rat (postnatal day 18); data as published in Michanski *et al*, 2023, stainings were for CtBP2/RIBEYE (magenta; labeling synaptic ribbons and IHC nuclei) and Bassoon (green; spots juxtaposing with ribbons represent IHC AZs, spots not juxtaposing with ribbons represent efferent synapses formed by lateral olivocochlear neurons onto SGN boutons). Scale bar = 5µm. **(ii)** Juxtaposing RIBEYE and Bassoon spots imaged in 2-D STED and confocal mode respectively. Scale bar = 500nm. Note the striking resemblance to reconstituted RIBEYE + palm-Bassoon structures in HEK293 cells as shown in **(Aii)**. STED images are from 3 sample transfections, representative of 7 total transfections; individual channels have been depicted with an intensity-coded look-up table with warmer colors indicating higher intensity.

C Quantification of RIBEYE and Bassoon signal intensity at periphery *vs* inside of cell shows a higher peripheral distribution of RIBEYE and Bassoon in HEK293 + RIBEYE + palm-Bassoon cells (N=9 cells) as compared to HEK293 + RIBEYE + Bassoon cells (N=9 cells); ****P < 0.0001, Mann-Whitney-Wilcoxon test. Overlaid data points represent individual cells, crosses represent mean values, central band indicates the median, whiskers represent 90/10 percentiles, and boxes represent 75/25 percentiles.

D Distribution of volumes of RIBEYE and palm-Bassoon puncta from HEK293 cells expressing RIBEYE and palm-Bassoon (n = 20 cells, quantifications from 5 sample transfections). Volumes of synaptic ribbons from rat IHCs (n = 29 cells, 3 rats) have been plotted for comparison.

245 **E** Box plot depicting data from **(D)**. Volumes of RIBEYE and palm-Bassoon puncta are comparable to
246 each other ($P > 0.99$, Kruskal-Wallis test with *post hoc* Dunn's multi-comparison), but on an
247 average much smaller and considerably more variable when compared to volumes of RIBEYE and
248 Bassoon puncta from rat IHCs respectively (*****P* < 0.0001, Kruskal-Wallis test with *post hoc*
249 Dunn's multi-comparison). Overlaid plus signs represent individual spots, crosses represent mean
250 values, central band indicates the median, whiskers represent 90/10 percentiles and boxes
251 represent 75/25 percentiles.

252 **F** RIBEYE puncta in HEK cells expressing RIBEYE and palm-Bassoon (n_{spots} = 864, N = 20 cells) appear
253 more spherical than Bassoon puncta in the same cells (n_{spots} = 961, N = 20 cells; *****P* < 0.0001,
254 Kruskal-Wallis test with *post hoc* Dunn's multiple comparison test). Note the similar trend in IHC
255 synaptic ribbons where RIBEYE puncta are more spherical than Bassoon puncta (n_{spots} = 290 for
256 RIBEYE and n_{spots} = 314 for Bassoon, N = 29 cells, 3 rats; *****P* < 0.0001, Kruskal-Wallis test with
257 *post hoc* Dunn's multiple comparison test). Overlaid plus signs represent individual spots, crosses
258 represent mean values, central band indicates the median, whiskers represent 90/10 percentiles
259 and boxes represent 75/25 percentiles.

260

261 Nonetheless, the fact that next to structures with volumes comparable to IHC ribbons, we also
262 encountered smaller and larger structures, likely reflects poorer regulation of RIBEYE and palm-
263 Bassoon expression in the heterologous system. RIBEYE clusters constituting *SyRibbons* appeared more
264 spherical than the plate-like Bassoon structures in the same cells (sphericity $\Psi = 0.91 \pm 0.05$, n_{spots} =
265 864 for RIBEYE versus $\Psi = 0.86 \pm 0.07$, n_{spots}= 951 for Bassoon, data from N = 20 cells; *****P* < 0.0001,
266 Kruskal-Wallis test with *post hoc* Dunn's multiple comparison test). This follows the same trend as in
267 rat IHCs where RIBEYE spots indeed appear more spherical ($\Psi = 0.90 \pm 0.05$, n_{spots} = 290) compared to
268 Bassoon spots ($\Psi = 0.76 \pm 0.10$, n_{spots} = 314); *****P* < 0.0001, Kruskal-Wallis test with *post hoc* Dunn's
269 multiple comparison test, data from N = 29 cells (Figure 2F).

270

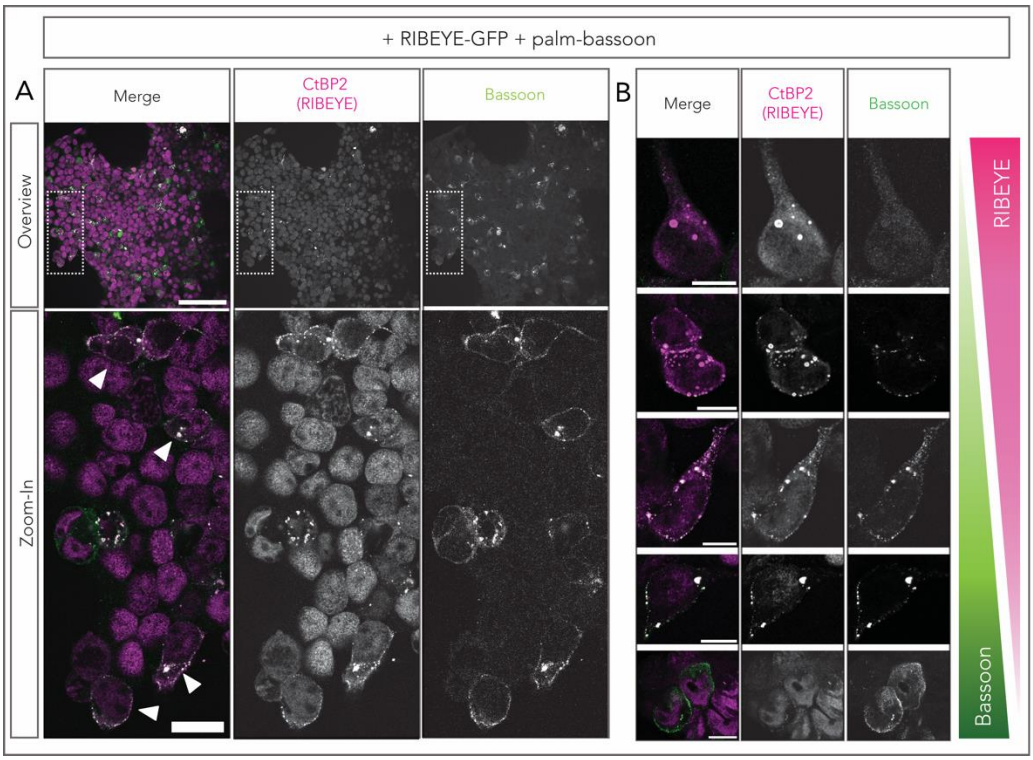

Figure EV2 - Membrane localization of RIBEYE depends on expression levels of palm-Bassoon

A Exemplary overview image of HEK293 cells co-transfected with RIBEYE (magenta) and palm-Bassoon (green) showing how to identify cells with *SyRibbons*. On an average about 10% of cells appear co-transfected of which some show peripheral distribution of RIBEYE (examples marked by arrows). Scale bar = 100 µm for overview and 20 µm for zoom-in.

B Peripheral distribution of RIBEYE appears to be dependent on expression levels of palm-Bassoon. Note the cell in the top panel with little to no palm-Bassoon expression and predominantly cytosolic RIBEYE puncta. Scale bar = 10 µm.

SyRibbons employ RBP2 to tether $Ca_V1.3$ channels.

To study the potential of *SyRibbons* to cluster Ca^{2+} channels, we employed HEK293 cells stably expressing an inducible transgene of $Ca_V1.3\alpha_1$ along with constitutive transgenes for $Ca_V\beta_3$ and $Ca_V\alpha_2\delta_1$. We either used tetracycline for inducible $Ca_V1.3\alpha_1$ channel expression (Fig 3A) or performed transient transfections with $Ca_V1.3$ constructs containing an N-terminal EGFP- (Fig 3B) or Halo-tag (Fig 3C) for direct fluorescence imaging. Expression of either Ca^{2+} channel complex resulted in small clusters at the plasma membrane as represented in Fig 3D (average volume 0.08 ± 0.13 µm^3, n_{spots} = 949, N = 12 cells for untagged inducible $Ca_V1.3\alpha_1$; 0.07 ± 0.08 µm^3, n_{spots} = 392, N = 11 cells for EGFP-$Ca_V1.3$; and 0.07 ± 0.09 µm^3, n_{spots} = 1281, N = 16 cells for Halo-$Ca_V1.3\alpha$; $P_{untagged/EGFP}$ = 0.547, $P_{untagged/Halo}$ > 0.999, $P_{Halo/EGFP}$ = 0.582, Kruskal-Wallis test with *post hoc* Dunn's multiple comparison test).

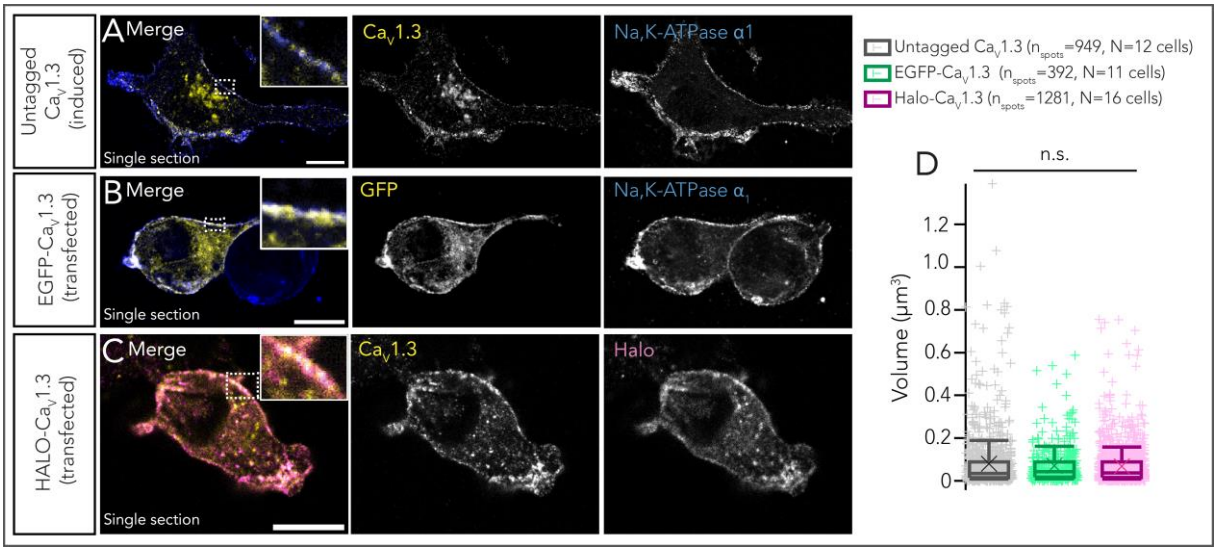

Figure 3 - HEK293 cells expressing $Ca_V1.3$

A Representative confocal section of a HEK293 cell stably expressing an inducible $Ca_V1.3\alpha$ transgene (untagged) along with constitutive transgenes for $Ca_V\beta_3$ and $Ca_V\alpha_2\delta_1$. Immunostainings have been performed using antibodies against $Ca_V1.3$ (green) and Na, K-ATPase α_1 (blue, labeling the plasma membrane). Scale bar = 10 µm.

B Representative confocal section of a HEK293 cell stably expressing $Ca_V\beta_3$ and $Ca_V\alpha_2\delta_1$, and transiently transfected with an N-terminal EGFP- tagged $Ca_V1.3$ construct. Immunostainings have been performed using antibodies against GFP (green) and Na, K-ATPase α_1 (blue). Scale bar = 10 µm.

C Representative confocal section of a HEK293 cell stably expressing $Ca_V\beta_3$ and $Ca_V\alpha_2\delta_1$ and transiently transfected with an N-terminal Halo-tagged $Ca_V1.3$ construct. Immunostainings have been performed using antibodies against $Ca_V1.3$ (green) and Halo tag (magenta). Scale bar = 10 µm.

D Expression of either of the Ca^{2+} channel complexes result in clusters of comparable sizes, ($P > 0.05$, Kruskal-Wallis test with *post hoc* Dunn's multiple comparison test). Overlaid plus signs represent individual spots, crosses represent mean values, central band indicates the median, whiskers represent 90/10 percentiles and boxes represent 75/25 percentiles.

Co-expression of palm-Bassoon did not show colocalization with $Ca_V1.3$, which is in line with observations with full-length Bassoon (Frank *et al*, 2010) and the same applied when co-expressing RIBEYE and $Ca_V1.3$, arguing against a direct interaction for both (Figure EV3). Rab-interacting molecule-binding protein (RIM-BP or RBP) links Bassoon to Ca^{2+} channels (Davydova *et al*, 2014) and hence was an interesting candidate for tethering $Ca_V1.3$ to Bassoon clusters. RBP has been shown to interact with $Ca_V1.3$ (Hibino *et al*, 2002) and to be required for normal $Ca_V1.3$ Ca^{2+} channel clustering at the IHC ribbon synapse (Krinner *et al*, 2017, 2021). Indeed, when co-expressing RBP2 with palm-Bassoon and $Ca_V1.3$, we found juxtaposed palm-Bassoon and $Ca_V1.3$ both with immunolabeled (Fig. 4A) and live-labeled (Fig. 4B, C) proteins indicating successful clustering of $Ca_V1.3$ at *synthetic* AZs.

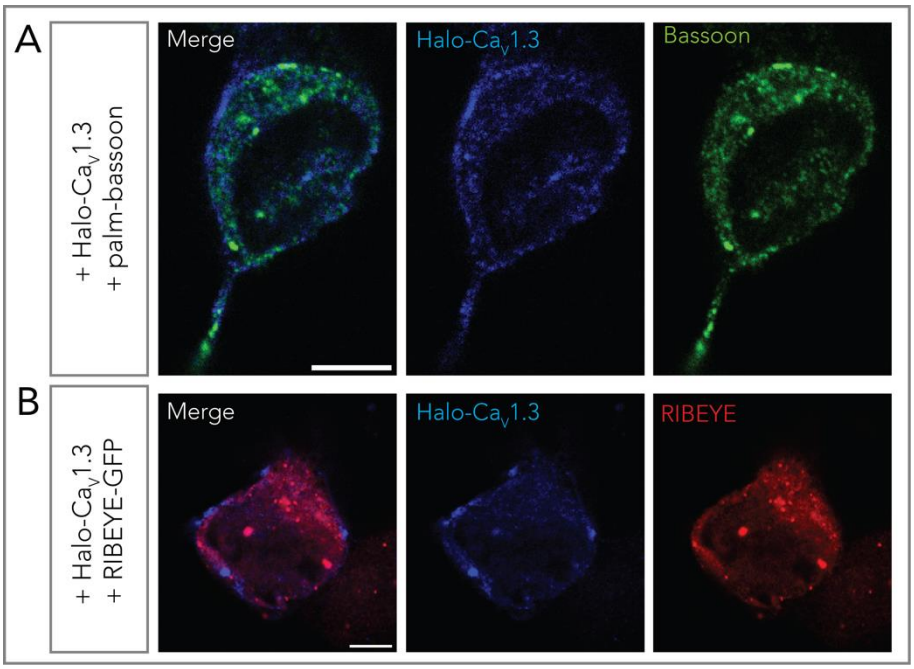

Figure EV3 - $Ca_V1.3$ does not appear to colocalize directly with RIBEYE or with palm-Bassoon

A Representative confocal section of a HEK293 cell transfected with Halo-$Ca_V1.3$ (blue) and palm-Bassoon (green). The two proteins do not appear to colocalize. Scale bar = 5 µm.

B Representative confocal section of a HEK293 cell transfected with Halo-$Ca_V1.3$ (blue) and RIBEYE-GFP (red). RIBEYE and $Ca_V1.3$ also do not appear to colocalize, speaking against a possible direct interaction between the two proteins. Scale bar = 5 µm.

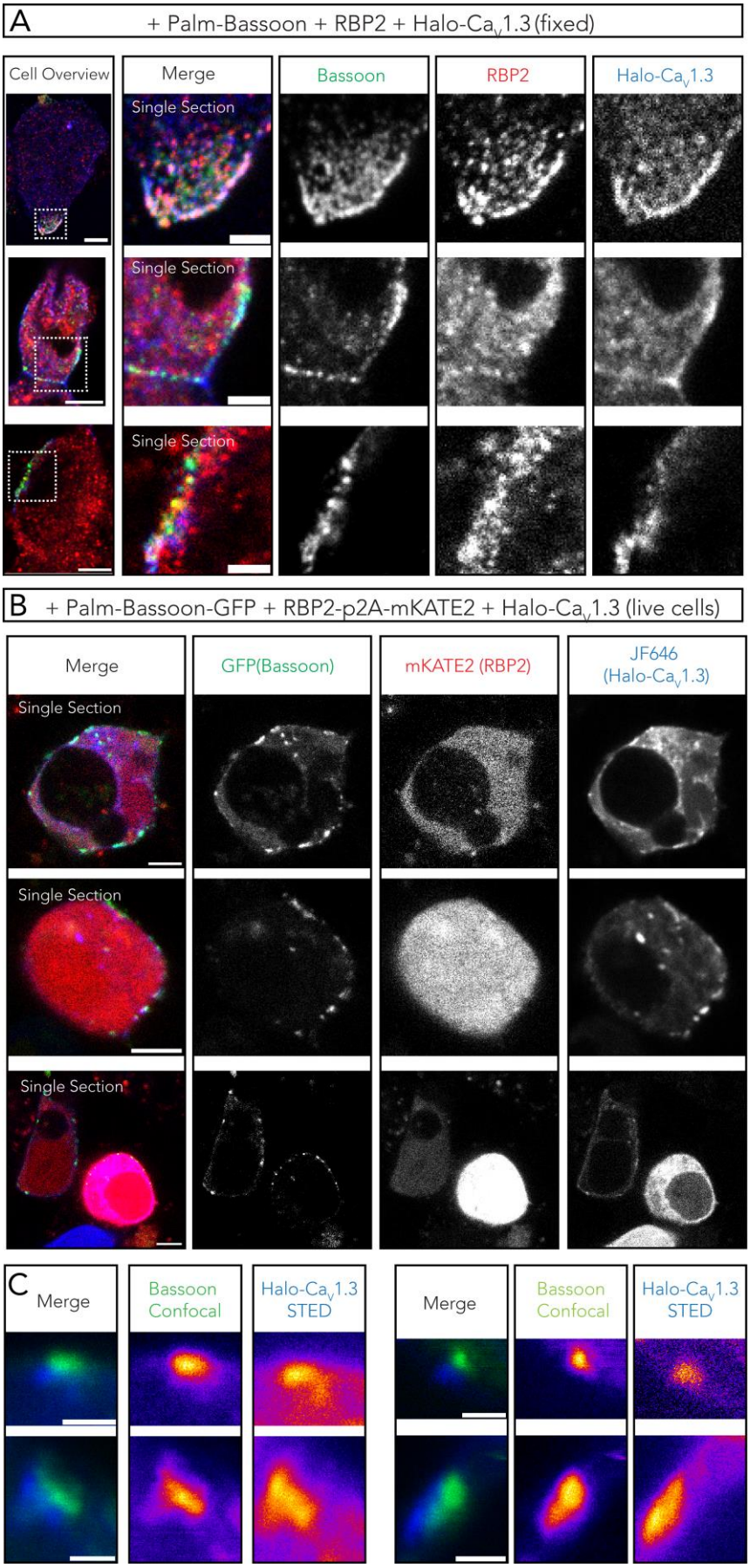
A
+ Palm-Bassoon + RBP2 + Halo-Ca$_V$1.3 (fixed)
Cell Overview
Merge
Bassoon
RBP2
Halo-Ca$_V$1.3
Single Section
Single Section
Single Section
B
+ Palm-Bassoon-GFP + RBP2-p2A-mKATE2 + Halo-Ca$_V$1.3 (live cells)
Merge
GFP(Bassoon)
mKATE2 (RBP2)
JF646
(Halo-Ca$_V$1.3)
Single Section
Single Section
Single Section
C
Merge
Bassoon
Confocal
Halo-Ca$_V$1.3
STED
Merge
Bassoon
Confocal
Halo-Ca$_V$1.3
STED

330 **Figure 4 – RBP2 bridges palm-Bassoon and $Ca_V1.3$ to form supra-molecular assemblies at the plasma**
331 **membrane.**

332 **A** Representative confocal images (single sections) of HEK293 cells (fixed) transfected with palm-
333 Bassoon (green), RBP2 (red) and N-terminal Halo-tagged $Ca_V1.3$ (blue). The three colocalizing
334 proteins appear to form supra-molecular assemblies at the cell membrane. Scale bar = 5 µm for
335 left panel showing cell overviews, 2 µm for right panels showing zoom-ins.

336 **B** Representative confocal images (single sections) of live HEK293 cells transfected with palm-
337 Bassoon-GFP (green), RBP2-p2A-mKATE2 (red, representing only mKATE2 signal and not RBP2
338 localization) and Halo-$Ca_V1.3$ (blue, labeled by with JF-646 HaloTag Ligand before imaging). Scale
339 bar = 5 µm.

340 **C** Exemplary super-resolution STED images from live-labeled samples in (B) showing juxtaposition
341 of palm-Bassoon and Halo-$Ca_V1.3$ signal at the plasma membrane in RBP2 positive cells. Scale bar
342 = 1 µm.

343

344 We next performed ruptured whole-cell patch-clamp to assess if RBP2 and/or palm-Bassoon or RIBEYE
345 co-expression results in changes in $Ca_V1.3$ Ca^{2+} currents. After tetracycline treatment for $Ca_V1.3\alpha_1$
346 expression (18-24 hours), cells were transfected with both RBP2-p2A-mKATE2 and palm-Bassoon-GFP,
347 with only palm-Bassoon-GFP, only RBP2-p2A-mKATE2 or RIBEYE-GFP constructs (Figure 5A). After 18-
348 24 hours, the cell culture media was changed, and cells were recorded 24-36 hours afterwards. We
349 used 10 mM $[Ca^{2+}]_e$ and recorded Ca^{2+} current (density) - voltage relations (IVs) ~1 minute after
350 establishing the whole-cell configuration by applying step depolarizations of 20 ms from -86.2 mV to
351 58.8 mV in 5 mV increments. Ca^{2+} current density was on an average approximately twice as large in
352 cells expressing both RBP2 and palm-Bassoon when compared with induced-only controls (Figure 5B,
353 D; ***P* = 0.0041, Kruskal-Wallis test with *post hoc* Dunn's multiple comparison test). Ca^{2+} current
354 densities also tended to be larger for cells expressing only palm-Bassoon or RBP2, but this difference
355 was not statistically significant (*P* = 0.374 and 0.164 respectively, Kruskal-Wallis test with *post hoc*
356 Dunn's multiple comparison test), while for cells expressing RIBEYE there was no trend to differ (P >
357 0.999, Kruskal-Wallis test with *post hoc* Dunn's multiple comparison test). We did not observe any
358 noticeable differences in voltage-dependence, activation kinetics or inactivation kinetics of $Ca_V1.3$ Ca^{2+}
359 current upon expression of any of these AZ proteins (Figure 5C, E, F; Figure EV4A, B).

360

361

362

363

364

365

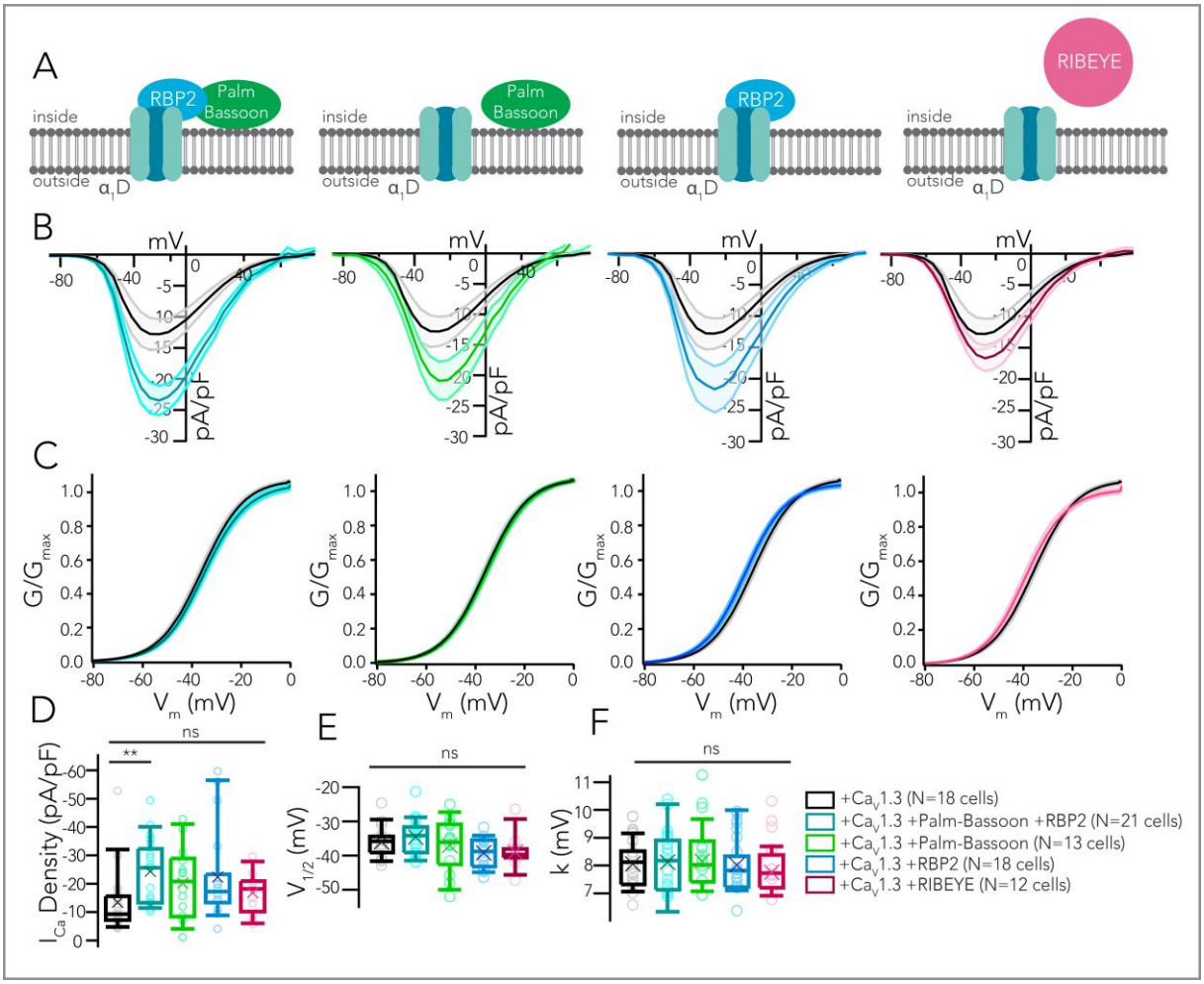

Figure 5 - Whole-cell Ca^{2+} current amplitudes increase upon co-expression of RBP2 and palm-Bassoon.

A Impact of co-expression of different ribbon-type AZ proteins on $Ca_V1.3\alpha_1/\beta_3/\alpha_2\delta_1$ Ca^{2+} currents. Color code: non-transfected controls expressing only $Ca_V1.3$ (black), co-expression of RBP2 + palm-Bassoon (data depicted in turquoise), only palm-Bassoon (green), only RBP2 (blue) or only RIBEYE (magenta). Numbers of recorded cells/group have been indicated in the figure (bottom right).

B Co-expression of RBP2 and palm-Bassoon seemingly increases the whole-cell Ca^{2+} current density in HEK293 cells expressing $Ca_V1.3$, $[Ca]_e$ = 10mM. Expression of palm-Bassoon or RBP2 individually also results in a mild increase, but this trend is not statistically significant as shown in (D). Expression of RIBEYE by itself causes no change in Ca^{2+} current density. Plots show lines representing mean Ca^{2+} current density traces and shaded area represents ± SEM.

C We fitted a Boltzmann function to traces in (B) to determine the fractional activation of $Ca_V1.3$ channels. The voltage-dependence of Ca^{2+} current influx does not appear to be different for any of the four scenarios.

D Box plot depicting peak Ca^{2+} current density values from (A). P values are as follows: $^{**}P_{CaV\ only/CaV+RBP2+PBsn} = 0.0041$, $P_{CaV\ only/CaV+PBsn} = 0.3737$, $P_{CaV\ only/CaV+RBP2} = 0.1643$, $P_{CaV\ only/CaV+RIBEYE} > 0.999$; Kruskal-Wallis test with *post hoc* Dunn's multiple comparison test.

E,F Box plots depicting voltage of half-maximal activation (V_{half}) and slope (k) of the Boltzmann fits in (C) show no statistically significant differences.

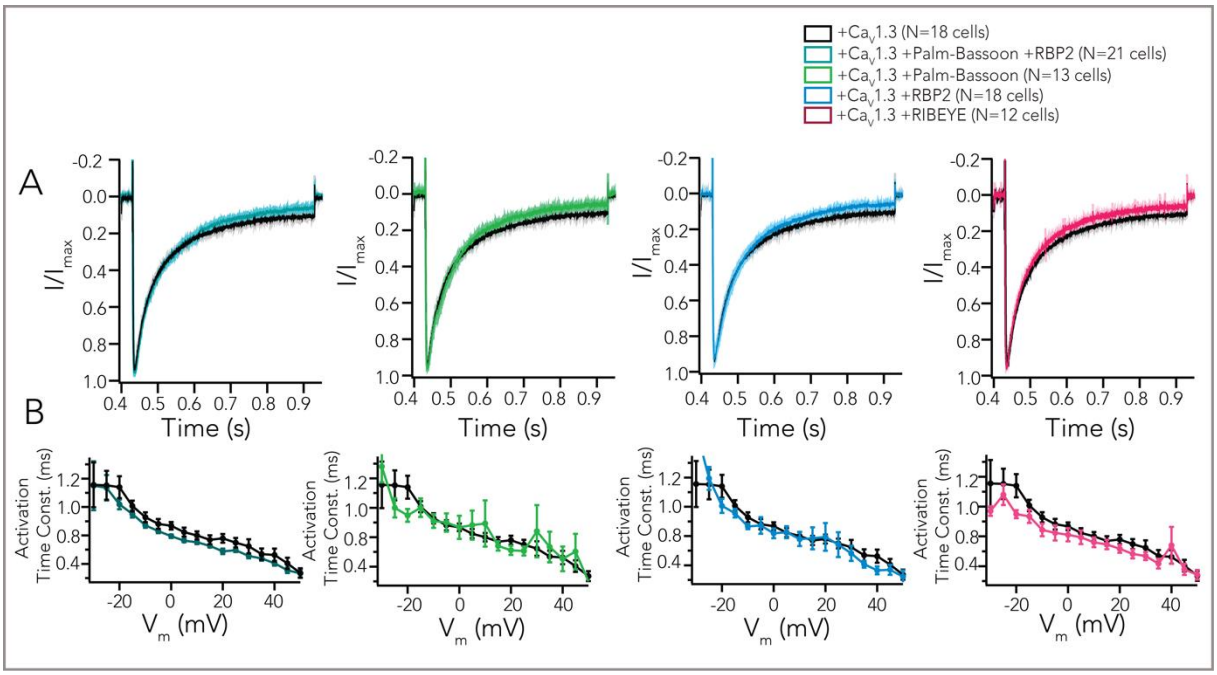

Figure EV4 - Kinetics of $Ca_V1.3$ channels are not altered upon co-expression of various AZ proteins.

A Average peak amplitude normalized Ca^{2+} current traces in response to depolarizations of 500 ms from -91.2 to -21.2 mV (shaded area represents ± SEM). Expression of palm-Bassoon+RBP2 (turquoise), only palm-Bassoon (green), RBP2 (blue) or RIBEYE (magenta) do not seem to impact inactivation of $Ca_V1.3$ channels.

B A power exponential function was fitted to the first 5 ms of current traces (as shown in Figure 5B) to obtain the activation time constant (mean ± SEM) at different voltages, which do not appear to be notably impacted.

Larger synthetic ribbon-type AZs establish larger $Ca_V1.3$ Ca^{2+} channel clusters.

Next, we tetra-transfected HEK293 cells with palm-Bassoon, Halo-tagged $Ca_V1.3\alpha_1$, RBP2 and RIBEYE to explore the impact of co-expressing of RIBEYE on the clustering of $Ca_V1.3$ Ca^{2+} channels (Figure 6A for transfection scheme). Using confocal imaging of immunofluorescently labelled RIBEYE, Halo-$Ca_V1.3$ and Bassoon (RBP2 immunofluorescence was imaged using epifluorescence to select tetra-transfected HEK293 cells), we observed colocalization of $Ca_V1.3\alpha1$, Bassoon and RIBEYE (Fig. 6B). Line profiles drawn tangentially along the plasma membrane showed that beyond the general distribution of a $Ca_V1.3\alpha_1$ signal in the plasma membrane, $Ca_V1.3\alpha_1$ signal hotspots occurred underneath the *SyRibbons* (Fig. 6C). The signal intensity of RIBEYE immunofluorescence positively correlated with the $Ca_V1.3$ signal immunofluorescence, (P_r = 0.839 and 0.886 from two sample line scans, ****P < 0.0001), which has previously been reported for immunolabeled native ribbon-type AZs of mouse IHCs (Ohn *et al*, 2016). We next turned to 2-color STED imaging which provided improved spatial resolution and highlighted the confined localization of $Ca_V1.3$ Ca^{2+} -channel clusters underneath *SyRibbons* as shown in Figure 6D.

412 We performed surface renderings of confocally imaged Halo-tagged $Ca_V1.3\alpha_1$, RIBEYE and palm-
413 Bassoon immunofluorescence spots as described above for estimating the volume of *SyRibbons* and
414 the $Ca_V1.3$ Ca^{2+} channel clusters (Fig.6E, F). This revealed significantly larger $Ca_V1.3$ Ca^{2+} channel
415 clusters when colocalizing with *SyRibbons* in HEK293 + Halo-$Ca_V1.3$ + RBP2 + *SyRibbons* cells (average
416 volume ± SD = 0.18 ± 0.28 μm^3, n_{spots}= 634, N = 13 cells, data representative of 5 transfections)
417 compared to non-colocalized $Ca_V1.3$ Ca^{2+} channel clusters from the same cells (volume = 0.06 ± 0.10
418 μm^3, n_{spots}= 1354, N = 13 cells; ****P < 0.0001, Kruskal-Wallis test with *post hoc* Dunn's multiple
419 comparison test) and $Ca_V1.3$ Ca^{2+} clusters in HEK293 cells solely expressing Halo-$Ca_V1.3$ Ca^{2+} channels
420 (volume = 0.07 ± 0.09μm^3, n_{spots}= 1281, N = 16 cells, data representative of 4 transfections; ****P <
421 0.0001, Kruskal-Wallis test with *post hoc* Dunn's multiple comparison test). $Ca_V1.3$ Ca^{2+} channel cluster
422 volumes in the latter two did not differ significantly (P = 0.099, Kruskal-Wallis test with *post hoc* Dunn's
423 multiple comparison test). Moreover, volumes of $Ca_V1.3$ cluster surfaces show a moderate positive
424 correlation with volumes of corresponding RIBEYE surfaces (P_r = 0.385, ****P < 0.0001), similar to
425 previous observations at IHC ribbon synapses (Frank *et al*, 2009; Michanski *et al*, 2023; Ohn *et al*, 2016).

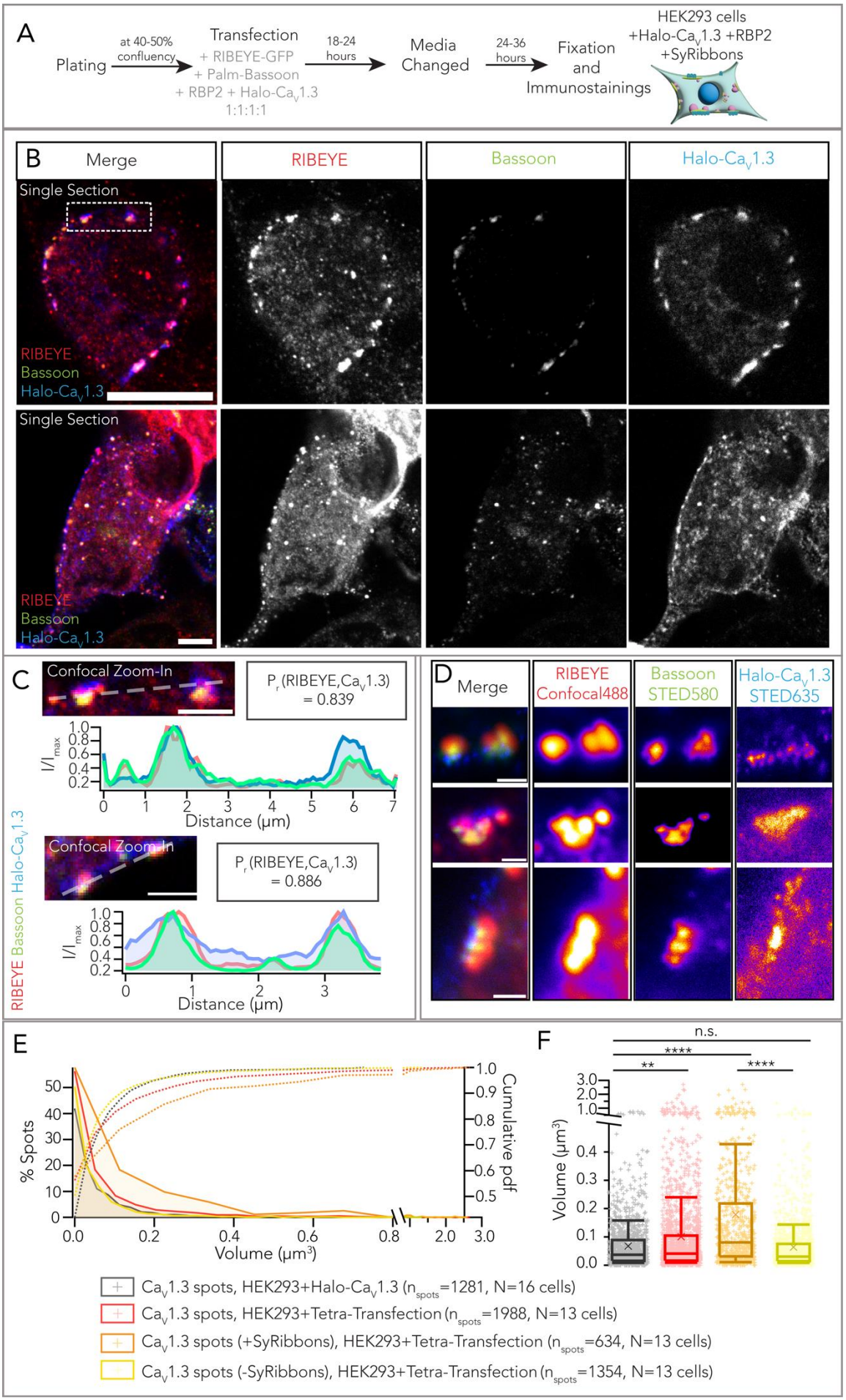
A
Plating
at 40-50% confluency
Transfection
+ RIBEYE-GFP
+ Palm-Bassoon
+ RBP2 + Halo-CaV1.3
1:1:1:1
18-24 hours
Media Changed
24-36 hours
Fixation and Immunostainings
HEK293 cells
+Halo-CaV1.3 +RBP2
+SyRibbons
B
Merge
RIBEYE
Bassoon
Halo-CaV1.3
Single Section
RIBEYE
Bassoon
Halo-CaV1.3
C
Confocal Zoom-In
Pr(RIBEYE,CaV1.3) = 0.839
I/Imax
Distance (µm)
Confocal Zoom-In
Pr(RIBEYE,CaV1.3) = 0.886
RIBEYE Bassoon Halo-CaV1.3
D
Merge
RIBEYE Confocal488
Bassoon STED580
Halo-CaV1.3 STED635
E
% Spots
Cumulative pdf
Volume (µm³)
F
n.s.
****
**
****
Volume (µm³)
CaV1.3 spots, HEK293+Halo-CaV1.3 (nspots=1281, N=16 cells)
CaV1.3 spots, HEK293+Tetra-Transfection (nspots=1988, N=13 cells)
CaV1.3 spots (+SyRibbons), HEK293+Tetra-Transfection (nspots=634, N=13 cells)
CaV1.3 spots (-SyRibbons), HEK293+Tetra-Transfection (nspots=1354, N=13 cells)

427
428 **Figure 6 - Synthetic ribbon-type active zones recruit $Ca_V1.3$ Ca^{2+} channels.**

429 **A** Experimental scheme for expression of Halo tagged $Ca_V1.3$, palm-Bassoon, RIBEYE-GFP and RBP2
430 in HEK293 cells.

431 **B** Representative confocal images (single sections) of HEK293 cells transfected with RBP2 (not
432 shown, expression confirmed using epifluorescence), RIBEYE-GFP (red), palm-Bassoon (green),
433 Halo-$Ca_V1.3$ (blue) shows colocalization of the three latter proteins at the plasma membrane. Scale
434 bar = 5 µm.

435 **C** Confocal zoom-ins from **(B)**. Line scans depict an increased $Ca_V1.3$ signal intensity (blue) at sites
436 where RIBEYE (red) and palm-Bassoon (green) clusters localize. Pearson's correlation coefficients
437 (*Pr*) were calculated along the line profiles for RIBEYE and $Ca_V1.3$ signal intensity and indicate a
438 high degree of correlation (~0.8) between the spatial localization of the two. Scale bar = 2 µm.

439 **D** Super-resolution STED images showing $Ca_V1.3$ clusters localizing at the base of the *SyRibbons*.
440 Scale bar = 500nm.

441 **E** Distribution of volumes from confocal images of $Ca_V1.3$ clusters colocalizing with *SyRibbons*
442 (orange, n_{spots} = 634) and not colocalizing with *SyRibbons* (yellow, n_{spots} = 1354) from HEK293 cells
443 expressing $Ca_V1.3$, RBP2 and *SyRibbons* (N = 13 cells). Pooled volumes of all $Ca_V1.3$ clusters (with
444 and without *SyRibbons*) from these cells have been shown in red (n_{spots} = 1988). Volumes of $Ca_V1.3$
445 clusters from HEK293 cells expressing only Halo-$Ca_V1.3$ (black, n_{spots} = 1281, N = 16 cells) have been
446 plotted for comparison.

447 **F** Box plot depicting data from (E). $Ca_V1.3$ clusters appear larger on an average in cells expressing
448 $Ca_V1.3$, RBP2 and *SyRibbons versus* in cells expressing only $Ca_V1.3$, (***P* = 0.0044). Within cells
449 expressing all four proteins, $Ca_V1.3$ clusters are much larger when colocalizing with *SyRibbons*
450 versus when they do not (*****P < 0.0001*,). Finally, when comparing these clusters with and
451 without *SyRibbons* in cells expressing all four proteins *versus* clusters in cells expressing only
452 $Ca_V1.3$, we observe a significant difference for the former (*****P < 0.0001*,), but not the latter (*P*
453 = 0.099,). Statistical test: Kruskal-Wallis test with *post hoc* Dunn's multiple comparison correction.
454 Overlaid plus signs represent individual spots, crosses represent mean values, central band
455 indicates the median, whiskers represent 90/10 percentiles and boxes represent 75/25
456 percentiles.

457

458 **Ca^{2+} imaging reveals increased Ca^{2+} signal intensity at synthetic ribbon-type active zones.**

459 Finally, we set-out to functionally characterize synthetic ribbon-type AZs. We combined patch-clamp
460 recordings of $Ca_V1.3$ Ca^{2+} influx with spinning-disk confocal microscopy to visualize Ca^{2+} signals at the
461 synthetic ribbon-type AZs in HEK293 cells. Following tetracycline-induction for $Ca_V1.3$ expression,
462 HEK293 cells were co-transfected with constructs expressing RIBEYE-GFP, untagged palm-Bassoon and
463 RBP2-p2A-mKATE2, (Figure 7A). We recorded mKATE2 positive cells that expressed peripheral GFP
464 puncta, indicative of RIBEYE and palm-Bassoon co-expression. We employed peripheral GFP
465 expression as a proxy of *SyRibbons* for functional analysis (Figure 7B). Ruptured patch-clamp recordings
466 were performed with 10 mM $[Ca^{2+}]_e$ and 10 mM intracellular EGTA to enhance the signal to background
467 ratio for visualizing Ca^{2+} influx using the low-affinity red-shifted Ca^{2+} indicator Calbryte590 (100 µM, k_d
468 = 1.4 µM). After loading the cell for approximately a minute, we first applied step depolarizations of
469 20 ms from -83 to +62 mV in 5-mV step increments to measure Ca^{2+} current (density)–voltage relations.

470 We did not observe any changes in either the Ca^{2+} current density (*P* = 0.293, t-test) or the voltage-
471 dependence of Ca^{2+} current (*P* = 0.780, t-test when comparing V_{half}) when comparing cells expressing
472 $Ca_V1.3$ + RBP2 + *SyRibbons* with cells expressing only $Ca_V1.3$ (Figure 7C and 7D). Next, we applied a
473 depolarizing pulse to +2 mV for 500 ms and acquired images at a frame rate of 20 Hz (Figure 7E). The
474 intracellular Ca^{2+} signals mediated by $Ca_V1.3$ Ca^{2+} influx were visualized as an increase in Calbryte590
475 fluorescence. The increase of Calbryte590 fluorescence appeared to spread throughout the HEK293
476 cell membrane with discrete regions of higher signal intensity at sites underneath the *SyRibbons*
477 (exemplary cell shown in Figure 7F with zoom-in at site with *SyRibbon* shown in 7G). We note that we
478 did not find noticeable red fluorescence at *SyRibbons* in the absence of depolarization, which is similar
479 to findings with Fluo-4FF in IHCs (Frank *et al*, 2009), but different from the situation for the large
480 spherical presynaptic bodies in bullfrog hair cells that are stained by Fluo-3 (Issa & Hudspeth, 1996).
481 Line profiles drawn tangentially to the membrane in composite ΔF image of Calbryte590 signal and
482 RIBEYE-GFP showed a high correlation between the localization of *SyRibbons* and peak intensity of
483 Calbryte590 fluorescence increase, indicating preferential Ca^{2+} signaling at the *SyRibbons* (two
484 representative line scans shown in Figure 7H, Pearson correlation coefficients of 0.783 and 0.757).
485 Recordings were made from 24 cells (7 transfections) and ROIs (diameter = 2 µm) at regions with and
486 without *SyRibbons* were analyzed as shown in Figure 7I. Calbryte590 $\Delta F_{max}/F_0$ values were calculated
487 for each ROI which on an average showed higher $\Delta F_{max}/F_0$ values for ROIs with *SyRibbons* (on average
488 ~26% higher) than for ROIs without *SyRibbons* (**P* = 0.018, paired t-test, Figure 7J). We note that
489 occasionally in some cells we observed a higher Calbryte590 signal increase at sites without *SyRibbons*,
490 and we attribute this to the likely presence of AZ-like clusters composed of RBP2 and palm-Bassoon in
491 these regions which we could not visualize.

492

493

494

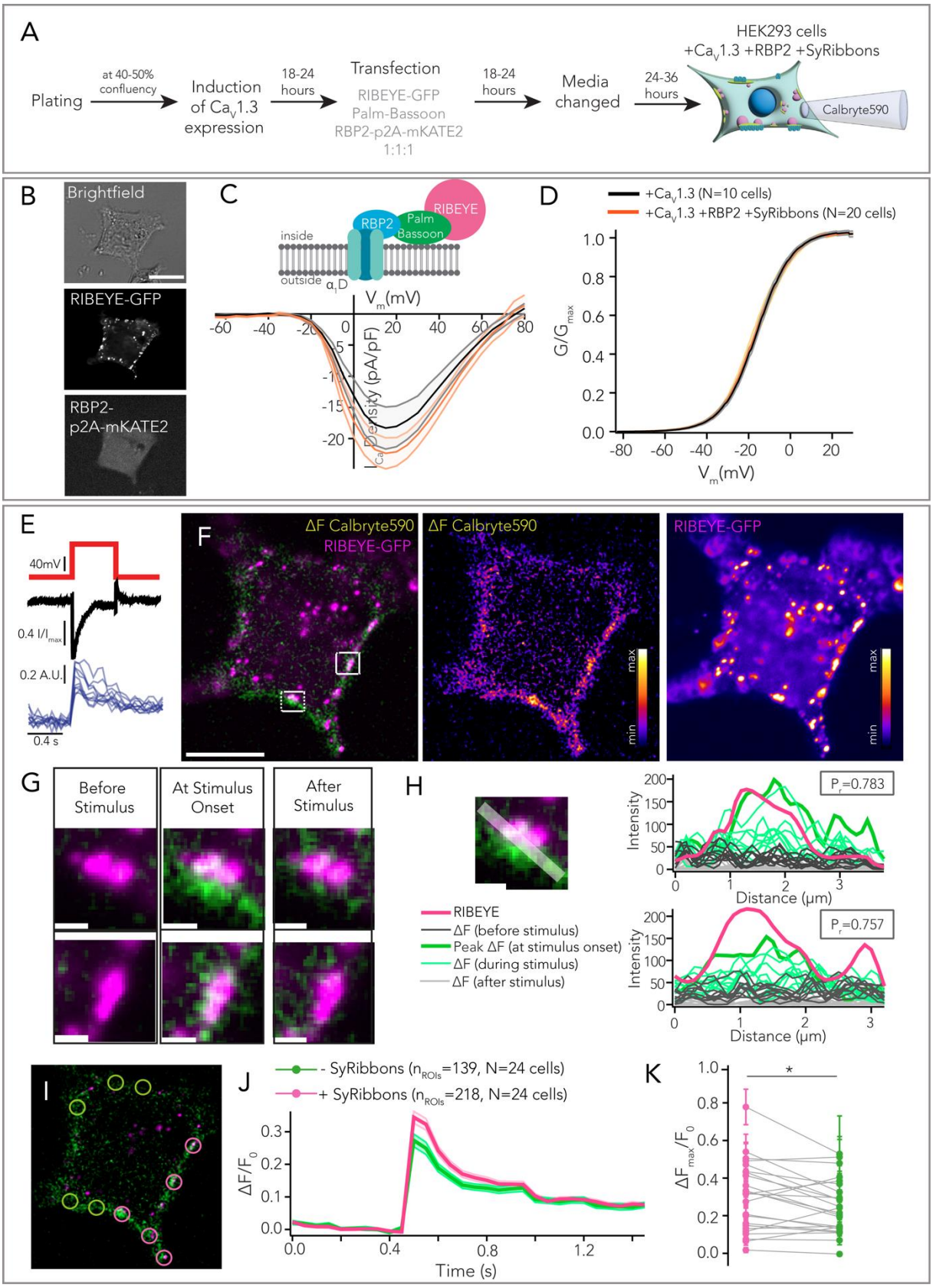

Figure 7 - Ca^{2+} imaging reveals higher Ca^{2+} signal intensity underneath *SyRibbons.*

A Experimental scheme for expression of *SyRibbons*, RBP2 and $Ca_V1.3$ in HEK293 cells for patch clamp in combination with Ca^{2+} imaging using the low affinity Ca^{2+} indicator Calbryte590.

499 **B** Exemplary cell used for Ca^{2+} imaging. Cells were identified by peripheral RIBEYE-GFP puncta
500 as shown (indicative of RIBEYE and palm-Bassoon co-expression) and mKATE2 signal
501 (indicative of RBP2 expression).

502 **C** Current density-voltage (IV) relations from whole-cell patch clamp recordings of HEK293 cells
503 expressing $Ca_V1.3$ + RBP2 + *SyRibbons* (n=20, in orange) and only $Ca_V1.3$ (n=10, in black). Lines
504 represent mean current traces, shaded area represents ± SEM. Whole-cell Ca^{2+} current density
505 does not appear to change upon co-expression of RBP2 and *SyRibbons* (P = 0.293, t-test).

506 **D** The voltage-dependence of Ca^{2+} current influx does not seem to be altered upon co-
507 expression of RBP2 and *SyRibbons* at the whole-cell level.

508 **E** A depolarizing pulse to +2mV was applied to the cells for 500 ms and the increase in
509 Calbryte590 fluorescence was measured by acquiring images at a frame rate of 20 Hz using a
510 spinning disk confocal microscope.

511 **F** Representative image of a HEK293 cell expressing *SyRibbons*, RBP2 and $Ca_V1.3$ stimulated as
512 described in (E). RIBEYE-GFP signal has been shown in magenta; the change in Calbryte590
513 fluorescence intensity (ΔF) upon Ca^{2+} binding (the frame at the onset of depolarization to
514 +2mV) has been shown in green. Note the distinct Ca^{2+} signal "hotspots" that co-localize with
515 *SyRibbons*. Scale bar = 10 µm.

516 **G** Zoom-ins from (F). Frames before, at the onset of, and after stimulation have been shown.
517 Note the localized Ca^{2+} influx at the base of the *SyRibbons*. Scale bar = 1 µm.

518 **H** Line profiles drawn tangentially to the membrane in composite ΔF image of Calbryte590 signal
519 and RIBEYE-GFP show a high correlation between the localization of *SyRibbons* and peak
520 intensity of Calbryte590 fluorescence increase (P_r = ~0.7). Plots show intensity profiles along
521 line scans for RIBEYE-GFP (magenta) and Calbryte590 (light grey for frames before stimulus,
522 bold green for peak intensity at onset of stimulus, light green lines for decaying intensity
523 during ongoing stimulus and dark grey for frames post-stimulus).

524 **I** Regions of interest (ROIs) of 2 µm diameter were drawn at sites with (magenta circles) and
525 without (green circles) *SyRibbons* and the corresponding Calbryte590 $\Delta F/F_0$ values were
526 calculated for each ROI.

527 **J** Plot of average (shaded area represents ± SEM) $\Delta F/F_0$ values from ROIs with and without
528 *SyRibbons* (218 and 139 ROIs respectively from N = 24 cells, data from 7 transfections).

529 **K** On average, Calbryte590 $\Delta F_{max}/F_0$ was higher for ROIs with *SyRibbons* than ROIs without them
530 in a given cell (*P = 0.018, paired t-test). Dots represent mean of $\Delta F_{max}/F_0$ from ROIs with
531 (magenta) and without (green) *SyRibbons* averaged per cell, error bars represent ± SEM.

532

533

534 ## Discussion

535 In this study, we reconstituted and characterized a minimal ribbon-type AZ model system using
536 heterologous expression. Co-expressing $Ca_V1.3$ Ca^{2+} channels with membrane targeted Bassoon for
537 RIBEYE anchorage to the plasma membrane and attracting exogenous RBP2 for clustering Ca^{2+}
538 channels in HEK293 cells led to structures recapitulating basic aspects of IHC ribbon synapses. Despite
539 the poor regulation of transgene expression in the synapse-naïve HEK293 cells, the AZ-like structures,
540 in the subset of cells were similar in morphology to the native IHC AZs. This applied to the *synthetic*
541 ribbons as well as to the AZ-like clusters of Bassoon, RBP2 and $Ca_V1.3$ Ca^{2+} channels. However, all three
542 components exhibited variability beyond the substantial natural heterogeneity found among the IHC
543 AZs (Moser *et al*, 2023). Functionally, Bassoon and RBP2 co-expression resulted in larger whole-cell
544 $Ca_V1.3$ currents. While additional expression of RIBEYE does not seem to enhance whole-cell Ca^{2+}
545 currents, we demonstrate a stronger, localized Ca^{2+} influx at *SyRibbons*. As *SyRibbons* partially
546 resemble native hair cell AZs, we expect this easily available and experimentally accessible system to
547 serve as an advanced testbed for functional interactions of AZ proteins and Ca^{2+} channels. Further
548 efforts towards reconstituting synaptic vesicles and their release sites will help to enhance the utility
549 of these synthetic AZs.

550

551 ### Synthetic active zone reconstitution model to study ribbon synapse assembly

552 By demonstrating that membrane-targeted Bassoon suffices to anchor ribbon-like RIBEYE assemblies,
553 this work adds to the top-down and bottom-up evidence for a key role of Bassoon in attracting RIBEYE
554 to the presynaptic density at the AZ in photoreceptors and hair cells (Dick *et al*, 2003; Khimich *et al*,
555 2005; Jing *et al*, 2013; tom Dieck *et al*, 2005). Additional expression of multi-domain proteins of the
556 presynaptic density such as CAST (Ohtsuka *et al*, 2002; Inoue *et al*, 2006) might replace the need for
557 artificial palmitoylation of Bassoon for membrane targeting. Furthermore, our results support a model
558 of a bidirectional control of AZ size and shape by RIBEYE and proteins of the presynaptic density. The
559 amount of RIBEYE assembled in membrane localized *SyRibbons* appeared regulated strongly
560 contrasting the seemingly unregulated cytosolic RIBEYE assemblies dominating HEK293 cells in the
561 absence of membrane-targeted Bassoon. Vice versa, clusters of Bassoon at the plasma membrane
562 were larger at *SyRibbons* than in the absence of RIBEYE. Finally, the size of *SyRibbons* seemingly scaled
563 with the size of $Ca_V1.3$ and Bassoon clusters similar to what is observed in IHCs (Ohn *et al*, 2016). Such
564 a model is consistent with results from genetic perturbation of native ribbon synapses: i) disruption of
565 RIBEYE leads to a disintegration of Bassoon into smaller subclusters in IHCs (Jean *et al*, 2018), and ii)
566 disruption of CAST and ELKS reduces the size of the ribbon-type AZs in rod photoreceptors (tom Dieck
567 *et al*, 2012; Hagiwara *et al*, 2018). We speculate that achieving the full extent of large ribbon-type AZs
568 such as in rod photoreceptors as well as regulating the size of ribbon-type AZs at a specific synapse

569 according to the precise functional demands requires such a functional interplay between proteins of
570 the presynaptic density and RIBEYE. We note that other ribbon-resident proteins such as piccolino
571 likely contribute to this fine-tuning of the size and shape of ribbon-type AZs. Indeed, disruption of
572 piccolino in IHCs reduced the average ribbon size (Müller *et al*, 2019; Michanski *et al*, 2023). One
573 exciting example of ribbon synapse heterogeneity manifests itself in IHCs where synapses show a
574 spatial size gradient that likely relates to the diverse molecular and functional properties of the
575 postsynaptic SGNs (reviewed in Moser *et al*, 2023).

576 **Insights into presynaptic Ca^{2+} channel clustering and function**

577 Current discussion of the clustering of Ca_V Ca^{2+} channels offers two different models: low affinity
578 protein-protein interactions (e.g. Hibino *et al*, 2002; Kaeser *et al*, 2011) via specific domains and liquid-
579 liquid phase separation involving intrinsically disordered domains (e.g. Heck *et al*, 2019). Work on
580 ribbon synapses has considered several layers of organizing Ca_V Ca^{2+} channels at the AZ that seem more
581 compatible with the former model: i) macro-clustering to which the synaptic ribbon contributes as a
582 "super-scaffold" (Jean *et al*, 2018; Neef *et al*, 2018; Frank *et al*, 2010; Maxeiner *et al*, 2016), ii) tethering
583 and micro-clustering by RBPs, RIMs, CAST and ELKS (Liu *et al*, 2011; Grabner *et al*, 2015; Jung *et al*,
584 2015; Krinner *et al*, 2017; Luo *et al*, 2017; Hagiwara *et al*, 2018) and iii) nanoscale coupling of Ca_V Ca^{2+}
585 channels and SV release sites (Brandt, 2005; Jarsky *et al*, 2010; Wong *et al*, 2014; Maxeiner *et al*, 2016;
586 Özçete & Moser, 2021; Grabner & Moser, 2021; Jaime Tobón & Moser, 2023) for which a role of the
587 ribbon has been more controversial (e.g. Maxeiner *et al*, 2016; Grabner & Moser, 2021). MINFLUX
588 nanoscopy of rod photoreceptor AZs recently revealed a well-ordered double-line array topography of
589 Ca_V Ca^{2+} channels, RIM, Bassoon and ubMunc13-2 at the presynaptic membrane on both sides of the
590 ribbon (Grabner *et al*, 2022). Clearly, we could not fully reconstitute this complex organization with
591 the minimal set of molecular players at *syRibbons* in HEK293 cells. Yet, we demonstrate augmentation
592 of $Ca_V1.3$ Ca^{2+} currents and clusters by co-expression of RBP and Bassoon and a positive effect of
593 *syRibbons* on local Ca^{2+} signaling, recapitulating micro- and macro-clustering of $Ca_V1.3$ Ca^{2+} channels.
594 However, we note that the functional impact of ribbon-mediated macro-clustering of $Ca_V1.3$ Ca^{2+}
595 channels remains unclear at the moment. Our Ca^{2+} imaging data seems more reminiscent of previous
596 work on ribbon-type AZs of immature IHCs (Wong *et al*, 2014) where a broader distribution of $Ca_V1.3$
597 and ribbons go along with an immature state of the IHC AZs. One clear limitation of the synthetic AZ
598 system in HEK293 cells is the lack of SVs and the molecular machinery required for SV release.
599 Nonetheless, our work paves the way for future studies including stable co-expression of AZ proteins
600 including of the release site marker Munc13-1 (Sakamoto *et al*, 2018; Böhme *et al*, 2016) and potential
601 delivery of SV machinery via co-expression (Park *et al*, 2021) or from synaptosomes. Alternatively,
602 using neurosecretory cells such as pheochromocytoma cells (PC12) or adrenal chromaffin cells in
603 primary culture, offer the advantage of providing synaptic-like microvesicles and a large set of

604 components of the presynaptic machinery such that expression of exogenous proteins might be limited
605 to RIBEYE. On the other hand, the complex molecular background involving various types of Ca_V
606 channels will likely complicate the interpretation. Regardless, *SyRibbons* in cultured cells offer great
607 availability and as adherent cells, are well accessible to sophisticated analysis by techniques such
608 MINFLUX nanoscopy and cryo-electron tomography. Future use of polycistronic gene expression or
609 stable cell lines expressing all components could help make the system become even more widely
610 applicable.

611

612 Materials and Methods

613 HEK cell culture and transfections

614 In this study, we used human embryonic kidney (HEK293) cells stably expressing a tetracycline-
615 inducible human $Ca_V1.3$ pore forming α_1-D subunit transgene (CACNA1D, NM_000720.2), and showing
616 constitutive expression of $Ca_V\beta_3$ (CACNB3, NM_000725.2) and $Ca_V\alpha_2\delta$-1 (CACNA2D1, NM_000722.2).
617 The stably expressing cell line was acquired from Charles River Laboratories, Cleveland, Ohio, USA (Cat.
618 No. CT6232). The cells were cultured as per product protocols in Dulbecco's Modified Eagle Medium
619 (DMEM) containing GlutaMax, high glucose and pyruvate (Gibco, Life Tech., 31966047), supplemented
620 with 10% Fetal Bovine Serum (FBS; Gibco, Life Tech., A5256701) and 100 units/ml of Penicillin-
621 Streptomycin (Gibco, Life Tech., 15070063). Additionally, the media was supplemented with 0.6 µM of
622 Isradipine (Sigma Aldrich, I6658) and the following selection antibiotics (in mg/ml): 0.005 Blasticidin
623 (Invivogen, ant-bl-05), 0.50 Geneticin (G418 Sulfate; Gibco, Life Tech., 10131027), 0.10 Zeocin
624 (InvivoGen, ant-zn-05) and 0.04 Hygromycin (Thermo Fisher, 10687010). Cells were cultured in a
625 humidified incubator at 37˚C with 5% (v/v) CO_2 saturation. Cells were split at ~70% confluency every
626 3-4 days to prevent adverse effects on cell growth and channel expression, by dissociating the cell
627 using Accutase (Sigma-Aldrich, A6964). The passage number did not exceed more than 26 passages.
628 For experiments, cells were grown in media lacking selection antibiotics. For induction of α_1-D subunit
629 expression, cells were treated with selection antibiotic-free medium containing 3 µg/ml tetracycline.
630 For transfection, 6.8 µg polyethylenimine (PEI, 25kDa linear, Polysciences, 23966) was added along
631 with a total of 2 µg of DNA to a final volume of 100 µl of DMEM (without FBS). The PEI/DNA mixture
632 was thoroughly mixed and allowed to incubate for 30 min at room temperature before being added to
633 the cells (30 µl/well in a 24-well-plate containing 500 µl media, cell confluency ~50-70%). For all
634 experiments with co-transfections, we used an equimolar ratio of DNA (total amount of DNA was kept
635 2 µg in a 100 µl transfection mix). After 18-24 hours, transfection media was replaced with fresh media
636 devoid of selection antibiotics. Cells were used for experiments (immunocytochemistry, patch clamp
637 and Ca^{2+} imaging) 24-48 hours after changing the media or as specified. If cell confluency was too high,

638 cells were reseeded to an appropriate confluency and allowed to settle for at least 12 hours before
639 commencement of experiments.
640
641 ## Expression vectors for RIBEYE, Bassoon, $Ca_V1.3$ and RBP2
642 **Table EV1: List of plasmids**

Plasmid Name	Backbone	Promoter	Insert	Antibiotic Resistance	Regulatory Elements	Reference
RIBEYE-GFP	pAAV-GFP	CMV-HBA	human RIBEYE-GFP	Ampicillin	WPRE	
Bassoon	pCS2+	CMV	Rat Bassoon	Kanamycin	SV40 poly(A)	
Palm-Bassoon-GFP	pEGFP-C1	CMV enhancer	Palm-rat Bassoon (95-3938)-EGFP	Kanamycin	SV40 poly(A)	
Palm-Bassoon-STOP	pEGFP-C1	CMV enhancer	Palm-rat Bassoon (95-3938)-STOP	Kanamycin	SV40 poly(A)	
EGFP-$Ca_V1.3$	pHTN	CMV enhancer-promoter	EGFP-human *CACNA1D*	Ampicillin	SV40 poly(A)	(Schwenzer *et al*, 2024)
Halo-$Ca_V1.3$	pHTN	CMV enhancer-promoter	HaloTag-human *CACNA1D*	Ampicillin	SV40 poly(A)	
RBP2-p2A-mKATE2	f(syn)w	CMV enhancer	mKATE2-p2A-RBP2	Ampicillin	WPRE, SV40 poly(A)	
RBP2	pAAV	CMV enhancer-HBA	RBP2	Ampicillin	WPRE, SV40 poly(A)	

643
644 The RIBEYE-GFP construct used consisted of a human RIBEYE cDNA cloned inframe into a pAAV-GFP
645 vector driven by a hybrid CMV-enhancer-human-beta-actin promoter (CMV-HBA) and containing a
646 downstream Woodchuck Hepatitis Virus (WHV) Posttranscriptional Regulatory Element (WPRE) for
647 mRNA stabilization. All Bassoon constructs encode rat Bassoon. The untagged full-length constructs
648 were cloned in the pCS2+ vector. For the generation of palm-Bassoon constructs, we used a pEGFP-C1
649 vector backbone with a CMV promoter and kanamycin resistance cassette. The insert comprised of a
650 palmitoylation consensus sequence of GAP43
651 (ATGCTGTGCTGTATGAGAAGAACCAAACAGGTTGAAAAGAATGATGAGGACCAAAAGATTTCCGGACTCAGA
652 TCTCGAG), followed by a cDNA sequence encoding amino acids 95-3938 of rat Bassoon, and a C-
653 terminal monomeric GFP. For the untagged version, the GFP tag was replaced by a STOP codon. To

654 generate the Halo-Ca_V1.3 plasmid (Schwenzer *et al*, 2024), human Ca_V1.3 cDNA (accession number
655 NM_001128840.2) was de-novo synthesized and assembled into a HaloTag vector (Promega G7721)
656 using restriction cloning, thus encoding an N-terminal fusion of Ca_V1.3 to HaloTag linked by a 'GGS'
657 sequence. The analogous GFP-Ca_V1.3 plasmid was generated by exchanging the HaloTag sequence for
658 mEGFP using restriction cloning. The RBP2 construct with an mKATE2 tag comprised of an insert coding
659 for mouse RBP2 (accession ID NP_001074857.1) with a p2A cleavage site followed by a C-terminal
660 mKATE2 cloned inframe into a f(syn)w-mKATE2-p2A vector driven by a CMV promoter-enhancer and
661 containing downstream WPRE sequence. The untagged version was made by cloning the RBP2 cDNA
662 from this plasmid and replacing RIBEYE-GFP in the pAAV-CMV-HBA-RIBEYE-GFP-WPRE plasmid by in-
663 fusion cloning (Takara Bio USA, Inc.).
664
665 **Immunocytochemistry and Imaging**
666 HEK293 cells plated on poly-L-lysine coated coverslips were fixed with 99% chilled methanol at -20˚C
667 for 2 minutes as previously described (Picher *et al*, 2017b). The coverslips were washed thoroughly
668 three times with PBS at room temperature (5 – 10 min). Blocking and permeabilization was performed
669 with GSDB (goat serum dilution buffer: 16% normal goat serum, 450 mM NaCl, 0.3% Triton X-100,
670 20mM phosphate buffer, pH ~7.4) for 45-60 minutes at room temperature. Samples were incubated
671 with respective primary antibodies (diluted in GSDB, refer to Table EV2) overnight at 4˚C or for 2 hours
672 at RT. The samples were then washed three times (5–10 minutes each) with wash buffer (450 mM
673 NaCl, 0.3% Triton X-100, 20mM phosphate buffer, pH ~ 7.4). Incubation with appropriate secondary
674 antibodies (also diluted in GSDB refer to Table EV2) was performed for 1 hour at room temperature in
675 a light-protected wet chamber. Lastly, the coverslips were washed three times with wash buffer (5-10
676 minutes each) and one final time with PBS, before mounting onto glass slides with a drop of
677 fluorescence mounting medium (Mowiol 4-88, Carl Roth). For live cell imaging of cells transfected with
678 Halo-Ca_V1.3 (Figure 4B, C), cells plated on glass-bottomed dishes were treated with Janelia Fluor 646
679 HaloTag Ligand (Promega, Cat. No. GA1120) at a final labelling concentration of 200nM (in cell culture
680 media). Cells were incubated with the ligand for ~60 min at 37˚C with 5% (v/v) CO_2 saturation, after
681 which the media was replaced with an equal volume of fresh warm culture media.
682 Images from fixed and live samples were acquired in confocal/ STED mode using an Olympus IX83
683 inverted microscope combined with an Abberior Instruments Expert Line STED microscope (Abberior
684 Instruments GmbH). We used lasers at 488, 561, and 633 nm for excitation and a 775 nm (1.2W) laser
685 for stimulated emission depletion. 1.4 NA 100X or 20X oil immersion objectives were used for fixed
686 samples, and a water immersion 60X objective was used for live samples. Confocal stacks or single
687 sections were acquired using *Imspector* Software (pixel size = 80 X 80 nm along xy, 200 nm along z).
688 For 2D-STED images, a pixel size of 15 X 15 nm (in xy) was used. Images in figure EV2A were acquired

689 using a Leica SP8 confocal microscope (Leica Microsystems, Germany). All acquired images were
690 visualized using NIH ImageJ software and adjusted for brightness and contrast. Samples and their
691 corresponding controls were processed in parallel using identical staining protocols, laser excitation
692 powers and microscope settings.
693
694 **Table EV2: List of antibodies**

Antibody	Host specie	Company	Dilution	Identifier
Anti-GFP	Chicken	Abcam	1:200	Ab13970
Anti-CtBP2	Mouse (monoclonal IgG1)	BD Biosciences	1:200	612044
Anti-RIBEYE-A	Guinea pig	Synaptic Systems	1:200	192104
Anti-RIBEYE-A	rabbit	Synaptic Systems	1:200	192103
Anti-RIBEYE-B	rabbit	Synaptic Systems	1:200	192003
Anti-Bassoon	chicken	Synaptic Systems	1:200	141016
Anti-Bassoon	mouse	Abcam	1:200	Ab82958
Anti-Na, K-ATPase α_1	mouse	Abcam	1:200	Ab7671
Anti-Calnexin	rabbit	Abcam	1:200	Ab22595
Anti-GM130	mouse	BD Biosciences	1:200	610822
Anti-LAMP1 (CD107A)	mouse	eBioscience	1:200	14-1079-80
Anti-Halo	mouse	Promega	1:200	G9211
Anti-RBP2	rabbit	Synaptic Systems	1:200	316103
Anti-$Ca_V1.3$	rabbit	Alomone	1:100	ACC005
Alexa Fluor 488 conjugated anti-chicken	Goat IgG (H+L)	Invitrogen	1:200	A11039
Alexa Fluor 488 conjugated anti-guinea pig	Goat IgG (H+L)	Invitrogen	1:200	A11073
Alexa Fluor 488 conjugated anti-rabbit	Goat IgG (H+L)	Invitrogen	1:200	A11008
Alexa Fluor 488 conjugated anti-mouse	Goat IgG (H+L)	Invitrogen	1:200	A11001
Alexa Fluor 405 conjugated anti-rabbit	Goat IgG (H+L)	Invitrogen	1:200	A31556

Alexa Fluor 546 conjugated anti-mouse	Goat IgG (H+L)	MoBiTec	1:200	A11003
Alexa Fluor 568 conjugated anti-chicken	Goat IgG (H+L)	Abcam	1:200	Ab175711
Alexa Fluor 568 conjugated anti-guinea pig	Goat IgG (H+L)	Invitrogen	1:200	A11075
Alexa Fluor 568 conjugated anti-rabbit	Goat IgG (H+L)	Thermo Fisher	1:200	A11011
Alexa Fluor 647 conjugated anti-mouse	Goat IgG (H+L)	Invitrogen	1:200	A21236
Alexa Fluor 647 conjugated anti-rabbit	Goat IgG (H+L)	Invitrogen	1:200	A21244
STAR Red conjugated anti-chicken	Goat IgY	Abberior	1:200	2-0102-011-2
STAR 635p conjugated anti-mouse	Goat IgG (H+L)	Abberior	1:200	ST635P-1001-500UG
STAR 635p conjugated anti-rabbit	Goat IgG (H+L)	Abberior	1:200	2-0012-007-2
STAR 580 conjugated anti-mouse	Goat IgG (H+L)	Abberior	1:200	ST580-1001-500UG

695

696 ## Patch clamp and calcium imaging

697 $Ca_V1.3$ stably expressing HEK293 cells were plated on coverslips till about 40-50% confluency was
698 achieved, following which they were induced for $Ca_V1.3\alpha1$-D expression by incubating them for 24-48
699 hours in induction media supplemented with tetracycline. For transfected cells, transfection was
700 performed after 24hrs of induction in the induction media as explained above. Cells were recorded in
701 extracellular solution containing (in mM): 150 choline-Cl, 10 HEPES, 1 $MgCl_2$ and 10 $CaCl_2$; pH was
702 adjusted to 7.3 with CsOH and osmolality was 300-310 mOsm/kg. For electrophysiological recordings
703 in Figure 5 and Figure S4, pipette solution contained (in mM): 140 NMDG, 10 NaCl, 10 HEPES, 5 EGTA,
704 3 Mg-ATP and 1 $MgCl_2$. pH was adjusted to 7.3 with methanesulfonic acid and osmolality was around

705 290 mOsm/kg. For Ca^{2+} imaging in Figure 7, the pipette solution contained (in mM): 111 Cs-glutamate,
706 1 $MgCl_2$, 1 $CaCl_2$, 10 EGTA, 13 TEA-Cl, 20 HEPES, 4 Mg-ATP, 0.3 Na-GTP, 1 L-glutathione, 0.1 Calbryte590
707 (AAT Bioquest, Cat. No. 20706); pH was adjusted to 7.3, osmolality to 290 mOsm/kg. Resistance of
708 patch pipettes was 3–7 MΩ. HEK293 cells were rupture patch clamped with EPC-10 amplifier (HEKA
709 electronics, Germany) controlled by *Patchmaster* software at room temperature, as described
710 previously (Picher *et al*, 2017b, 2017a). Cells were kept at a holding potential of -91.2 or -88 mV. All
711 voltages were corrected for liquid junction potential offline (21.2 mV or 18 mV). Currents were leak
712 corrected using a p/10 protocol. Recordings were discarded when leak current exceeded -50 pA, R_s
713 exceeded 15 MΩ or offset potential fluctuated more than 5 mV. Current voltage (IV) relations were
714 recorded around 1 minute after rupturing the cell, by applying increasing step-depolarisation pulses of
715 voltage ranging from -86.2 mV to 58.8 mV, in steps of 5 mV. Depolarisation pulses of 500 ms were used
716 for measure $Ca_V1.3$ inactivation in Figure EV4A.

717 For Ca^{2+} imaging experiments, we used a Yokogawa CSU-X1A spinning-disk confocal scanner, mounted
718 on an upright microscope (Zeiss Examiner) with a 63X, 1.0 NA objective (W Plan-Apochromat, Zeiss).
719 Images were acquired using an Andor Zyla sCMOS 4.2 camera, controlled by *VisiView* 5.0 software
720 (Visitron Systems GmbH). GFP, mKATE2 and the low-affinity Ca^{2+} indicator Calbryte590 were excited
721 by a VS Laser Merge System (Visitron Systems) with 488 and 561 nm laser lines. Spinning disk was set
722 to 5000 rpm. mKATE2 positive cells showing peripheral GFP expression (indicative of RIBEYE and palm-
723 Bassoon co-expression) were identified and used for recordings. The cell was loaded for approximately
724 a minute with Calbryte590 dye, after which we applied step depolarizations of 20 ms from -83 to +62
725 mV in 5-mV step increments to measure Ca^{2+} current (density)–voltage relations. Next, a central plane
726 of the cell was selected and the GFP fluorescence (green channel) of the cell showing *SyRibbons* was
727 imaged. This was immediately followed by imaging of the increments of Calbryte590 fluorescence (red
728 channel) in the same plane triggered by a depolarizing pulse to +2 mV for 500 ms (frame rate = 20 Hz).
729 For Ca^{2+} imaging experiments, we also included occasionally occurring HEK293 cells which were
730 electrically coupled with other neighbouring HEK293 cells. For such cells, we could not fully
731 compensate for the slow capacitive currents and we did not use them for electrophysiological analysis.

732 **Data analysis**

733

734 **Analysis of confocal images**

735 All images were processed using NIH ImageJ software to make z-projections and multi-channel
736 composites, and figures were created using Adobe Illustrator. For analysis of membrane distribution,
737 a region of interest (ROI) of 1 µm thickness was drawn along the periphery of the cell which was
738 identified either using Na, K ATPase α_1 immunofluorescence or by enhancing the contrast in images

739 of transfected cells so that the cell boundary becomes distinguishable. Mean pixel intensity was
740 measured along this ROI and for the area enclosed within the ROI. The ratio of the mean pixel
741 intensity (periphery: inside) per cell was reported as an average from at least three central planes;
742 we did not use the basal and top plane. For volumetric fits of *SyRibbons,* IHC ribbons and Ca^{2+} channel
743 clusters, we used the inbuilt surface detection algorithm from Imaris 9.6 (Oxford Instruments). The
744 surface detail was set to 0.16 µm and largest sphere diameters for background subtraction were set
745 as follows: for RIBEYE/CtBP2 0.3 µm, for Bassoon 0.1 µm and for $Ca_V1.3$ 0.08 µm. Thresholding was
746 performed based on the quality of immunofluorescence to ensure all discernible surfaces were
747 detected. All surfaces with less than 10 voxels were filtered out. A manual check was done to include
748 undetected surfaces, remove surfaces not localizing within cell of interest, and split surfaces that
749 would occasionally be clubbed together. For analysis of *SyRibbons*, only RIBEYE surfaces colocalizing
750 with palm-Bassoon surfaces were used for quantifications (at 0.06 µm or less). Occasionally we
751 would detect surfaces with volumes larger than 2 μm^3 (usually cytosolic) or smaller than 0.02 μm^3,
752 which were not considered for analysis. For $Ca_V1.3$ cluster volumetric analysis, clusters classified as
753 *+SyRibbons* were at 0.045 µm or less from palm-Bassoon positive RIBEYE surfaces. All other clusters
754 were classified as *–SyRibbons*. Only clusters localized at the periphery of the cell were used for
755 analysis.
756

757 **Analysis of patch clamp and Ca^{2+} imaging data**

758 Analysis of electrophysiology data and figure preparation was performed using Igor Pro 6 and 7
759 (WaveMetrics Inc.) and final figures were compiled using Adobe Illustrator. For analyzing current
760 density-voltage relations (IVs), the evoked Ca^{2+} current was averaged from 5 to 10 ms after
761 depolarization start. Cells expressing current amplitudes less than -49 pA and with current density
762 greater than -60 pA/pF were not taken into account for analysis.
763 Ca^{2+} imaging data analysis was performed using a customized script in ImageJ. Briefly, we performed
764 background subtraction in time series with Calbryte590 signal and then averaged 5 frames before
765 stimulation and subtracted these from an average of three frames during stimulation to obtain ΔF
766 images. For visualization, the images were smoothened (3 X 3 unweighted smoothening) and a
767 composite was created by overlaying the ΔF images and the RIBEYE-GFP channel. For analyzing $\Delta F/F_0$,
768 we drew circular regions of interest (ROIs) of 2µm diameter at sites with and without *SyRibbons* in the
769 background subtracted time series. The $\Delta F_{max}/F_0$ was calculated as the of average $\Delta F/F_0$ in first three
770 frames of peak Ca^{2+} signal intensity at stimulation onset in each ROI. To minimize bias while assigning
771 regions as with or without *SyRibbons*, ROIs were assigned in the RIBEYE-GFP channel, without looking
772 at the corresponding Calbryte590 signal.
773

774 ### Statistics

775 Data sorting and statistics were performed using MS Excel, *Igor Pro 7* and/or *GraphPad Prism 10*.
776 Numerical data is represented mainly as mean ± standard deviation (SD). The normality of data was
777 assessed using Jarque-Bera test and Kolmogorov-Smirnov test, and the equality of variances was
778 checked using *F*-test. When comparing two samples, a two-tailed unpaired Student's *t*-test (or paired
779 *t*-test for Figure 7J) was performed for normally distributed samples with equal variances. If the
780 conditions for normality and equality of variances were not met, an unpaired Mann-Whitney-Wilcoxon
781 test was performed. When comparing multiple samples, a one-way ANOVA with post hoc Tukey's test
782 was used for normally distributed data with equal variances. For samples which were not normally
783 distributed, we used Kruskal-Wallis test with *post hoc* Dunn's multi-comparison correction. All box
784 plots are depicted with crosses representing mean values, central bands indicating median, whiskers
785 for 90/10 percentiles, boxes for 75/25 percentiles and individual data points overlaid. Non-significant
786 differences have been indicated as n.s., while significant *P* values have been depicted as $*P$ for < 0.05,
787 $**P < 0.01$, $***P < 0.001$, and $****P < 0.0001$.
788

789 ## Acknowledgments:

790 We would like to thank Dr. Kathrin Kusch for advice on cloning, Dr. Jakob Neef for critical feedback on
791 the manuscript, and Nare Karagulyan for valuable discussions regarding Ca^{2+} imaging. We are grateful
792 to Sandra Gerke, Christiane Senger-Freitag, Sina Langer and Ina Preuss for expert technical assistance
793 and Patricia Räke-Kügler for the administrative support during this study. We would also like to thank
794 Prof. Erwin Neher and Prof. Silvio Rizzoli for their feedback throughout the course of this study. Lastly,
795 we would like to thank lab rotation students Gantavya Arora and Ugur Coskun for their initial
796 contributions to the project.
797

798 ## Funding:

799 RK was supported by funding from the Studienstiftung des Deutschen Volkes. This work was further
800 supported by funding of the European Union (ERC, "DynaHear", grant agreement No. 101054467),
801 Deutsche Forschungsgemeinschaft (DFG, German Research Foundation) via the EXC 2067/1 (MBExC)
802 to SEL and TM, and Fondation Pour l'Audition (FPA RD-2020-10).

803 **Author Contributions:** TM and RK designed the study. RK performed the experiments and the
804 analysis under supervision of TM. TD, NS and SEL prepared and characterized expression plasmids for
805 membrane targeted Bassoon (TD) and EGFP/Halo-tagged $Ca_V1.3\alpha1$ (NS, SEL). RK and TM prepared the
806 manuscript with contribution of all authors.

807 **Disclosure and Competing Interests Statement:** The authors declare that no competing
808 interests exist.
809

810 References

811 Ann Marie Craig, Ethan R. Graf, & Michael W. Linhoff (2006) How to build a central synapse: clues
812 from cell culture. *Trends Neurosci* Volume 29: 8–20

813 Becker L, Schnee ME, Niwa M, Sun W, Maxeiner S, Talaei S, Kachar B, Rutherford MA & Ricci AJ
814 (2018) The presynaptic ribbon maintains vesicle populations at the hair cell afferent fiber
815 synapse. *eLife* 7: e30241

816 Böhme MA, Beis C, Reddy-Alla S, Reynolds E, Mampell MM, Grasskamp AT, Lützkendorf J, Bergeron
817 DD, Driller JH, Babikir H, *et al* (2016) Active zone scaffolds differentially accumulate Unc13
818 isoforms to tune Ca^{2+} channel–vesicle coupling. *Nat Neurosci* 19: 1311–1320

819 Brandt A (2005) Few CaV1.3 Channels Regulate the Exocytosis of a Synaptic Vesicle at the Hair Cell
820 Ribbon Synapse. *J Neurosci* 25: 11577–11585

821 Brandt A, Striessnig J & Moser T (2003) Ca_V 1.3 Channels Are Essential for Development and
822 Presynaptic Activity of Cochlear Inner Hair Cells. *J Neurosci* 23: 10832–10840

823 Bunt AH (1971) Enzymatic digestion of synaptic ribbons in amphibian retinal photoreceptors. *Brain*
824 *Res* 25: 571–577

825 Davydova D, Marini C, King C, Klueva J, Bischof F, Romorini S, Montenegro-Venegas C, Heine M,
826 Schneider R, Schröder MS, *et al* (2014) Bassoon specifically controls presynaptic P/Q-type
827 Ca(2+) channels via RIM-binding protein. *Neuron* 82: 181–194

828 Dick O, tom Dieck S, Altrock WD, Ammermüller J, Weiler R, Garner CC, Gundelfinger ED &
829 Brandstätter JH (2003) The Presynaptic Active Zone Protein Bassoon Is Essential for
830 Photoreceptor Ribbon Synapse Formation in the Retina. *Neuron* 37: 775–786

831 tom Dieck S, Altrock WD, Kessels MM, Qualmann B, Regus H, Brauner D, Fejtová A, Bracko O,
832 Gundelfinger ED & Brandstätter JH (2005) Molecular dissection of the photoreceptor ribbon
833 synapse: physical interaction of Bassoon and RIBEYE is essential for the assembly of the
834 ribbon complex. *J Cell Biol* 168: 825–836

835 tom Dieck S, Sanmartí-Vila L, Langnaese K, Richter K, Kindler S, Soyke A, Wex H, Smalla KH, Kämpf U,
836 Fränzer JT, *et al* (1998) Bassoon, a novel zinc-finger CAG/glutamine-repeat protein selectively
837 localized at the active zone of presynaptic nerve terminals. *J Cell Biol* 142: 499–509

838 tom Dieck S, Specht D, Strenzke N, Hida Y, Krishnamoorthy V, Schmidt K-F, Inoue E, Ishizaki H,
839 Tanaka-Okamoto M, Miyoshi J, *et al* (2012) Deletion of the presynaptic scaffold CAST reduces
840 active zone size in rod photoreceptors and impairs visual processing. *J Neurosci* 32: 12192–
841 12203

842 Dou H, Vazquez AE, Namkung Y, Chu H, Cardell EL, Nie L, Parson S, Shin H-S & Yamoah EN (2004) Null
843 mutation of alpha1D Ca^{2+} channel gene results in deafness but no vestibular defect in mice. *J*
844 *Assoc Res Otolaryngol JARO* 5: 215–226

845 Edmonds BW (2004) Evidence that fast exocytosis can be predominantly mediated by vesicles not
846 docked at active zones in frog saccular hair cells. *J Physiol* 560: 439–450

847 Frank T, Khimich D, Neef A & Moser T (2009) Mechanisms contributing to synaptic Ca2+ signals and
848 their heterogeneity in hair cells. *Proc Natl Acad Sci* 106: 4483–4488

849 Frank T, Rutherford MA, Strenzke N, Neef A, Pangršič T, Khimich D, Fejtova A, Gundelfinger ED,
850 Liberman MC, Harke B, *et al* (2010) Bassoon and the synaptic ribbon organize Ca^{2+} channels
851 and vesicles to add release sites and promote refilling. *Neuron* 68: 724–738

852 Glowatzki E & Fuchs PA (2002) Transmitter release at the hair cell ribbon synapse. *Nat Neurosci* 5:
853 147–154

854 Grabner CP, Gandini MA, Rehak R, Le Y, Zamponi GW & Schmitz F (2015) RIM1/2-Mediated
855 Facilitation of Cav1.4 Channel Opening Is Required for Ca2+-Stimulated Release in Mouse
856 Rod Photoreceptors. *J Neurosci* 35: 13133–13147

857 Grabner CP, Jansen I, Neef J, Weihs T, Schmidt R, Riedel D, Wurm CA & Moser T (2022) Resolving the
858 molecular architecture of the photoreceptor active zone with 3D-MINFLUX. *Sci Adv* 8:
859 eabl7560

860 Grabner CP & Moser T (2021) The mammalian rod synaptic ribbon is essential for Cav channel
861 facilitation and ultrafast synaptic vesicle fusion. *eLife* 10: e63844

862 Graydon CW, Cho S, Li G-L, Kachar B & von Gersdorff H (2011) Sharp Ca2+ Nanodomains beneath the
863 Ribbon Promote Highly Synchronous Multivesicular Release at Hair Cell Synapses. *J Neurosci*
864 31: 16637–16650

865 Hagiwara A, Kitahara Y, Grabner CP, Vogl C, Abe M, Kitta R, Ohta K, Nakamura K, Sakimura K, Moser
866 T, *et al* (2018) Cytomatrix proteins CAST and ELKS regulate retinal photoreceptor
867 development and maintenance. *J Cell Biol* 217: 3993–4006

868 Heck J, Parutto P, Ciuraszkiewicz A, Bikbaev A, Freund R, Mitlöhner J, Andres-Alonso M, Fejtova A,
869 Holcman D & Heine M (2019) Transient Confinement of CaV2.1 Ca2+-Channel Splice Variants
870 Shapes Synaptic Short-Term Plasticity. *Neuron* 103: 66-79.e12

871 Heidelberger R, Heinemann C, Neher E & Matthews G (1994) Calcium dependence of the rate of
872 exocytosis in a synaptic terminal. *Nature* 371: 513–515

873 Hibino H, Pironkova R, Onwumere O, Vologodskaia M, Hudspeth AJ & Lesage F (2002) RIM - binding
874 proteins (RBPs) couple Rab3 - interacting molecules (RIMs) to voltage - gated Ca2+ channels.
875 *Neuron* 34: 411–423

876 Holt M, Cooke A, Neef A & Lagnado L (2004) High Mobility of Vesicles Supports Continuous
877 Exocytosis at a Ribbon Synapse. *Curr Biol* 14: 173–183

878 Inoue E, Deguchi-Tawarada M, Takao-Rikitsu E, Inoue M, Kitajima I, Ohtsuka T & Takai Y (2006) ELKS,
879 a protein structurally related to the active zone protein CAST, is involved in Ca2+-dependent
880 exocytosis from PC12 cells. *Genes Cells* 11: 659–672

881 Jaime Tobón LM & Moser T (2023) Ca2+ regulation of glutamate release from inner hair cells of
882 hearing mice. *Proc Natl Acad Sci* 120: e2311539120

883 Jarsky T, Tian M & Singer JH (2010) Nanodomain control of exocytosis is responsible for the signaling
884 capability of a retinal ribbon synapse. *J Neurosci Off J Soc Neurosci* 30: 11885–11895

885 Jean P, Morena DL de la, Michanski S, Tobón LMJ, Chakrabarti R, Picher MM, Neef J, Jung S, Gültas M,
886 Maxeiner S, *et al* (2018) The synaptic ribbon is critical for sound encoding at high rates and
887 with temporal precision. *eLife* 7: e29275

888 Jing Z, Rutherford MA, Takago H, Frank T, Fejtova A, Khimich D, Moser T & Strenzke N (2013)
889 Disruption of the presynaptic cytomatrix protein bassoon degrades ribbon anchorage,
890 multiquantal release, and sound encoding at the hair cell afferent synapse. *J Neurosci* 33:
891 4456–4467

892 Jung S, Oshima-Takago T, Chakrabarti R, Wong AB, Jing Z, Yamanbaeva G, Picher MM, Wojcik SM,
893 Göttfert F, Predoehl F, *et al* (2015) Rab3-interacting molecules 2α and 2β promote the
894 abundance of voltage-gated CaV1.3 Ca2+ channels at hair cell active zones. *Proc Natl Acad*
895 *Sci* 112: E3141–E3149

896 Kaeser PS, Deng L, Wang Y, Dulubova I, Liu X, Rizo J & Südhof TC (2011) RIM proteins tether Ca2+
897 channels to presynaptic active zones via a direct PDZ-domain interaction. *Cell* 144: 282–295

898 Khimich D, Nouvian R, Pujol R, tom Dieck S, Egner A, Gundelfinger ED & Moser T (2005) Hair cell
899 synaptic ribbons are essential for synchronous auditory signalling. *Nature* 434: 889–894

900 Krinner S, Butola T, Jung S, Wichmann C & Moser T (2017) RIM-Binding Protein 2 Promotes a Large
901 Number of CaV1.3 Ca2+-Channels and Contributes to Fast Synaptic Vesicle Replenishment at
902 Hair Cell Active Zones. *Front Cell Neurosci* 11: 334

903 Krinner S, Predoehl F, Burfeind D, Vogl C & Moser T (2021) RIM-Binding Proteins Are Required for
904 Normal Sound-Encoding at Afferent Inner Hair Cell Synapses. *Front Mol Neurosci* 14: 651935

905 Liu KSY, Siebert M, Mertel S, Knoche E, Wegener S, Wichmann C, Matkovic T, Muhammad K, Depner
906 H, Mettke C, *et al* (2011) RIM-binding protein, a central part of the active zone, is essential
907 for neurotransmitter release. *Science* 334: 1565–1569

908 Luo F, Liu X, Südhof TC & Acuna C (2017) Efficient stimulus-secretion coupling at ribbon synapses
909 requires RIM-binding protein tethering of L-type Ca^{2+} channels. *Proc Natl Acad Sci* 114:
910 E8081–E8090

911 Magupalli VG, Schwarz K, Alpadi K, Natarajan S, Seigel GM & Schmitz F (2008) Multiple RIBEYE-RIBEYE
912 interactions create a dynamic scaffold for the formation of synaptic ribbons. *J Neurosci Off J*
913 *Soc Neurosci* 28: 7954–7967

914 Matthews G & Fuchs P (2010) The diverse roles of ribbon synapses in sensory neurotransmission. *Nat*
915 *Rev Neurosci* 11: 812–822

916 Maxeiner S, Luo F, Tan A, Schmitz F & Südhof TC (2016) How to make a synaptic ribbon: RIBEYE
917 deletion abolishes ribbons in retinal synapses and disrupts neurotransmitter release. *EMBO J*
918 35: 1098–1114

919 Mehta B, Snellman J, Chen S, Li W & Zenisek D (2013) Synaptic Ribbons Influence the Size and
920 Frequency of Miniature-like Evoked Postsynaptic Currents. *Neuron* 77: 516–527

921 Michanski S, Kapoor R, Steyer AM, Möbius W, Früholz I, Ackermann F, Gültas M, Garner CC, Hamra
922 FK, Neef J, *et al* (2023) Piccolino is required for ribbon architecture at cochlear inner hair cell
923 synapses and for hearing. *EMBO Rep* 24: e56702

924 Michanski S, Smaluch K, Steyer AM, Chakrabarti R, Setz C, Oestreicher D, Fischer C, Möbius W, Moser
925 T, Vogl C, *et al* (2019) Mapping developmental maturation of inner hair cell ribbon synapses
926 in the apical mouse cochlea. *Proc Natl Acad Sci* 116: 6415–6424

927 Moser T, Grabner CP & Schmitz F (2019) Sensory processing at ribbon synapses in the retina and the
928 cochlea. *Physiol Rev* 100: 103–144

929 Moser T, Karagulyan N, Neef J & Jaime Tobón LM (2023) Diversity matters — extending sound
930 intensity coding by inner hair cells via heterogeneous synapses. *EMBO J* n/a: e114587

931 Müller TM, Gierke K, Joachimsthaler A, Sticht H, Izsvák Z, Hamra FK, Fejtová A, Ackermann F, Garner
932 CC, Kremers J, *et al* (2019) A multiple Piccolino-RIBEYE interaction supports plate-shaped
933 synaptic ribbons in retinal neurons. *J Neurosci* 39: 2038–18

934 Naoum P. Issa & A. J. Hudspeth (1996) Characterization of fluo-3 labelling of dense bodies at the hair
935 cell's presynaptic active zone. *J Neurocytol* 25: 257–266

936 Neef J, Urban NT, Ohn T-L, Frank T, Jean P, Hell SW, Willig KI & Moser T (2018) Quantitative optical
937 nanophysiology of Ca^{2+} signaling at inner hair cell active zones. *Nat Commun* 9: 290

938 Ohn T-L, Rutherford MA, Jing Z, Jung S, Duque-Afonso CJ, Hoch G, Picher MM, Scharinger A, Strenzke
939 N & Moser T (2016) Hair cells use active zones with different voltage dependence of Ca^{2+}
940 influx to decompose sounds into complementary neural codes. *Proc Natl Acad Sci* 113:
941 E4716–E4725

942 Ohtsuka T, Takao-Rikitsu E, Inoue E, Inoue M, Takeuchi M, Matsubara K, Deguchi-Tawarada M, Satoh
943 K, Morimoto K, Nakanishi H, *et al* (2002) Cast: a novel protein of the cytomatrix at the active
944 zone of synapses that forms a ternary complex with RIM1 and munc13-1. *J Cell Biol* 158: 577–
945 590

946 Özçete ÖD & Moser T (2021) A sensory cell diversifies its output by varying Ca^{2+} influx-release
947 coupling among active zones. *EMBO J* 40: e106010

948 Park D, Wu Y, Lee S-E, Kim G, Jeong S, Milovanovic D, Camilli PD & Chang S (2021) Cooperative
949 function of synaptophysin and synapsin in the generation of synaptic vesicle-like clusters in
950 non-neuronal cells. *Nat Commun* 12

951 Picher MM, Gehrt A, Meese S, Ivanovic A, Predoehl F, Jung S, Schrauwen I, Dragonetti AG, Colombo
952 R, Camp GV, *et al* (2017a) Ca2+-binding protein 2 inhibits Ca2+-channel inactivation in mouse
953 inner hair cells. *Proc Natl Acad Sci* 114: E1717–E1726

954 Picher MM, Oprişoreanu A-M, Jung S, Michel K, Schoch S & Moser T (2017b) Rab Interacting
955 Molecules 2 and 3 Directly Interact with the Pore-Forming CaV1.3 Ca2+ Channel Subunit and
956 Promote Its Membrane Expression. *Front Cell Neurosci* 11

957 Platzer J, Engel J, Schrott-Fischer A, Stephan K, Bova S, Chen H, Zheng H & Striessnig J (2000)
958 Congenital deafness and sinoatrial node dysfunction in mice lacking class D L-type Ca^{2+}
959 channels. *Cell* 102: 89–97

960 Sakamoto H, Ariyoshi T, Kimpara N, Sugao K, Taiko I, Takikawa K, Asanuma D, Namiki S & Hirose K
961 (2018) Synaptic weight set by Munc13-1 supramolecular assemblies. *Nat Neurosci* 21: 41–49

962 Schmitz F, Königstorfer A & Südhof TC (2000) RIBEYE, a component of synaptic ribbons: a protein's
963 journey through evolution provides insight into synaptic ribbon function. *Neuron* 28: 857–
964 872

965 Schwenzer N, Tsukanov R, Kohl T, Basak S, Seibertz F, Voigt N, Enderlein J & Lehnart SE (2024)
966 Nanoscale architecture and dynamics of CaV1.3 channel clusters in cardiac myocytes
967 revealed by single channel nanoscopy. *bioRxiv*

968 Singer JH, Lassová L, Vardi N & Diamond JS (2004) Coordinated multivesicular release at a
969 mammalian ribbon synapse. *Nat Neurosci* 7: 826–833

970 Snellman J, Mehta B, Babai N, Bartoletti TM, Akmentin W, Francis A, Matthews G, Thoreson W &
971 Zenisek D (2011) Acute destruction of the synaptic ribbon reveals a role for the ribbon in
972 vesicle priming. *Nat Neurosci* 14: 1135–1141

973 Vaithianathan T, Henry D, Akmentin W & Matthews G (2016) Nanoscale dynamics of synaptic vesicle
974 trafficking and fusion at the presynaptic active zone. *eLife* 5: e13245

975 Wong AB, Rutherford MA, Gabrielaitis M, Pangršič T, Göttfert F, Frank T, Michanski S, Hell S, Wolf F,
976 Wichmann C, *et al* (2014) Developmental refinement of hair cell synapses tightens the
977 coupling of Ca2+ influx to exocytosis. *EMBO J* 33: 247–264

978

979

980

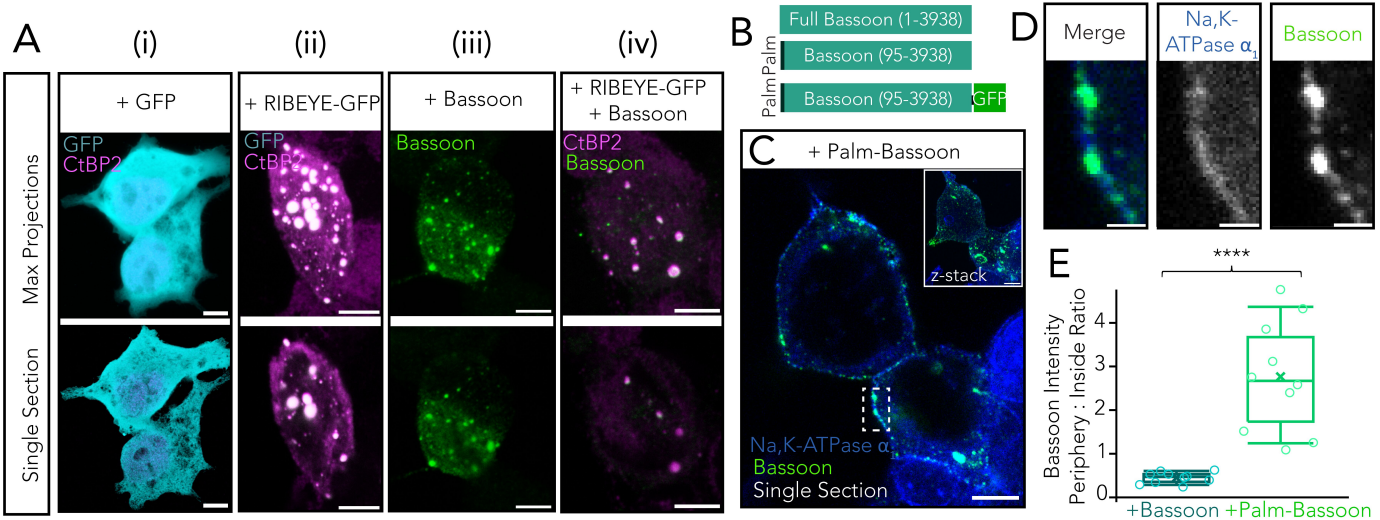
A
(i)
(ii)
(iii)
(iv)
+ GFP
+ RIBEYE-GFP
+ Bassoon
+ RIBEYE-GFP
+ Bassoon
Max Projections
Single Section
GFP
CtBP2
GFP
CtBP2
Bassoon
CtBP2
Bassoon
B
Full Bassoon (1-3938)
Palm
Bassoon (95-3938)
Palm
Bassoon (95-3938)
GFP
C
+ Palm-Bassoon
z-stack
Na,K-ATPase α1
Bassoon
Single Section
D
Merge
Na,K-ATPase α1
Bassoon
E
****
Bassoon Intensity
Periphery : Inside Ratio
0
1
2
3
4
+Bassoon
+Palm-Bassoon

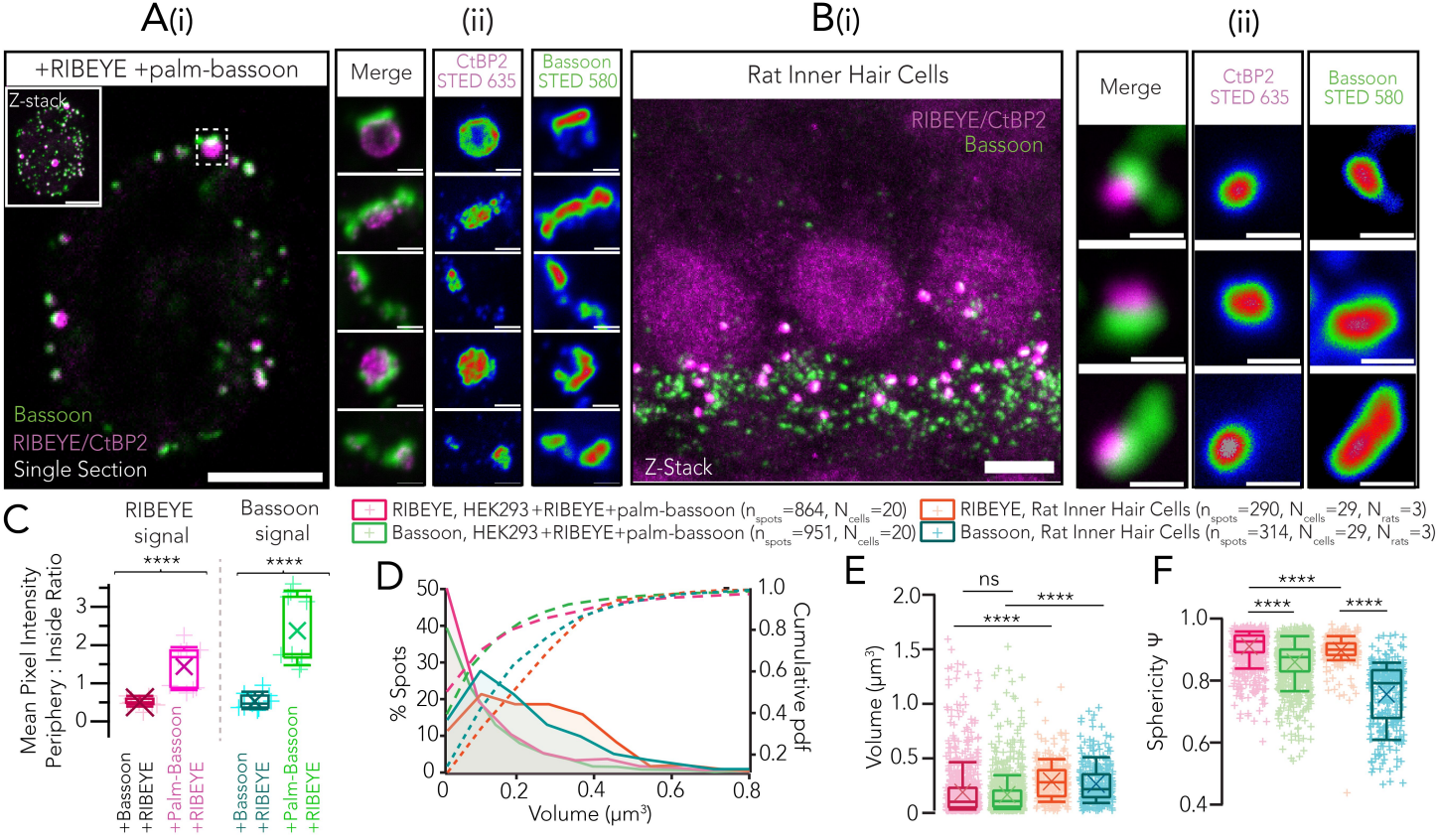
A(i)
(ii)
+RIBEYE +palm-bassoon
Z-stack
Bassoon
RIBEYE/CtBP2
Single Section
Merge
CtBP2 STED 635
Bassoon STED 580
B(i)
(ii)
Rat Inner Hair Cells
RIBEYE/CtBP2
Bassoon
Z-Stack
Merge
CtBP2 STED 635
Bassoon STED 580
C
RIBEYE signal
Bassoon signal
Mean Pixel Intensity Periphery : Inside Ratio
****
+Bassoon +RIBEYE
+Palm-Bassoon +RIBEYE
RIBEYE, HEK293+RIBEYE+palm-bassoon (n_spots=864, N_cells=20)
Bassoon, HEK293+RIBEYE+palm-bassoon (n_spots=951, N_cells=20)
RIBEYE, Rat Inner Hair Cells (n_spots=290, N_cells=29, N_rats=3)
Bassoon, Rat Inner Hair Cells (n_spots=314, N_cells=29, N_rats=3)
D
% Spots
Cumulative pdf
Volume (µm³)
E
Volume (µm³)
ns
****
F
Sphericity Ψ
****

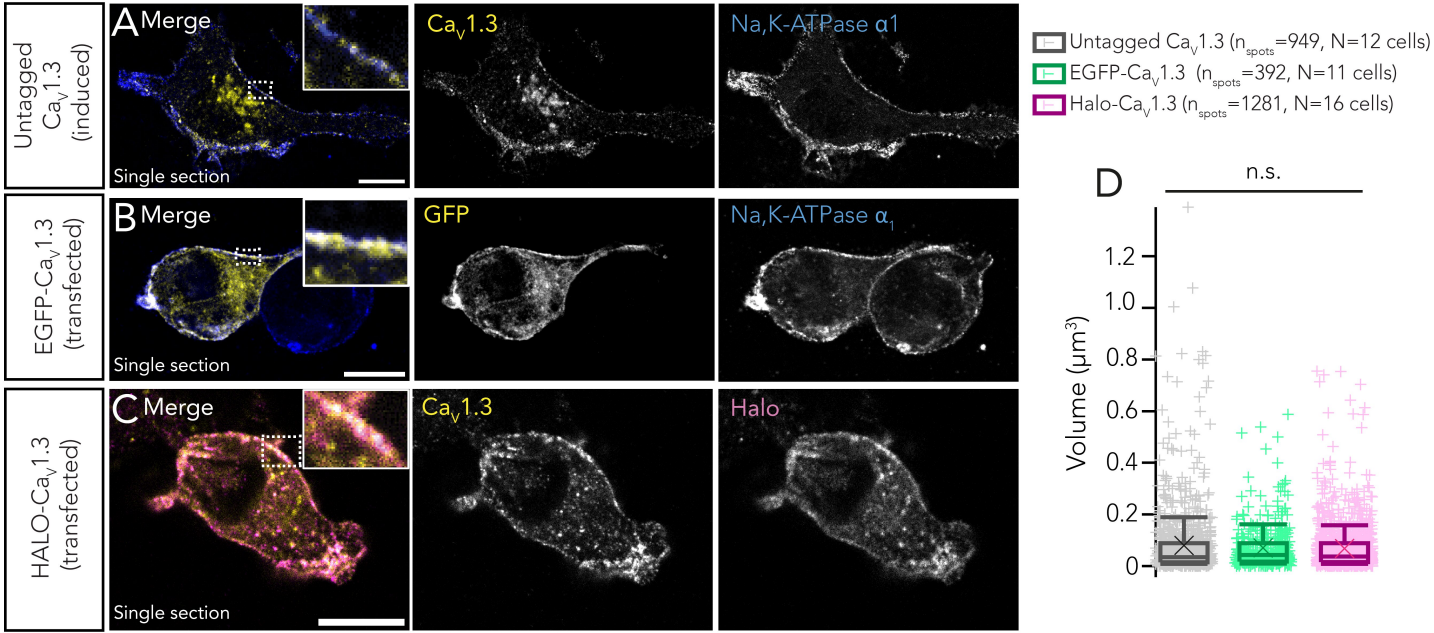
Untagged $Ca_V1.3$ (induced)
EGFP-$Ca_V1.3$ (transfected)
HALO-$Ca_V1.3$ (transfected)
A Merge
Single section
$Ca_V1.3$
Na,K-ATPase α1
B Merge
Single section
GFP
Na,K-ATPase $α_1$
C Merge
Single section
$Ca_V1.3$
Halo
Untagged $Ca_V1.3$ (n_{spots}=949, N=12 cells)
EGFP-$Ca_V1.3$ (n_{spots}=392, N=11 cells)
Halo-$Ca_V1.3$ (n_{spots}=1281, N=16 cells)
D
n.s.
Volume ($μm^3$)
1.2
1.0
0.8
0.6
0.4
0.2
0

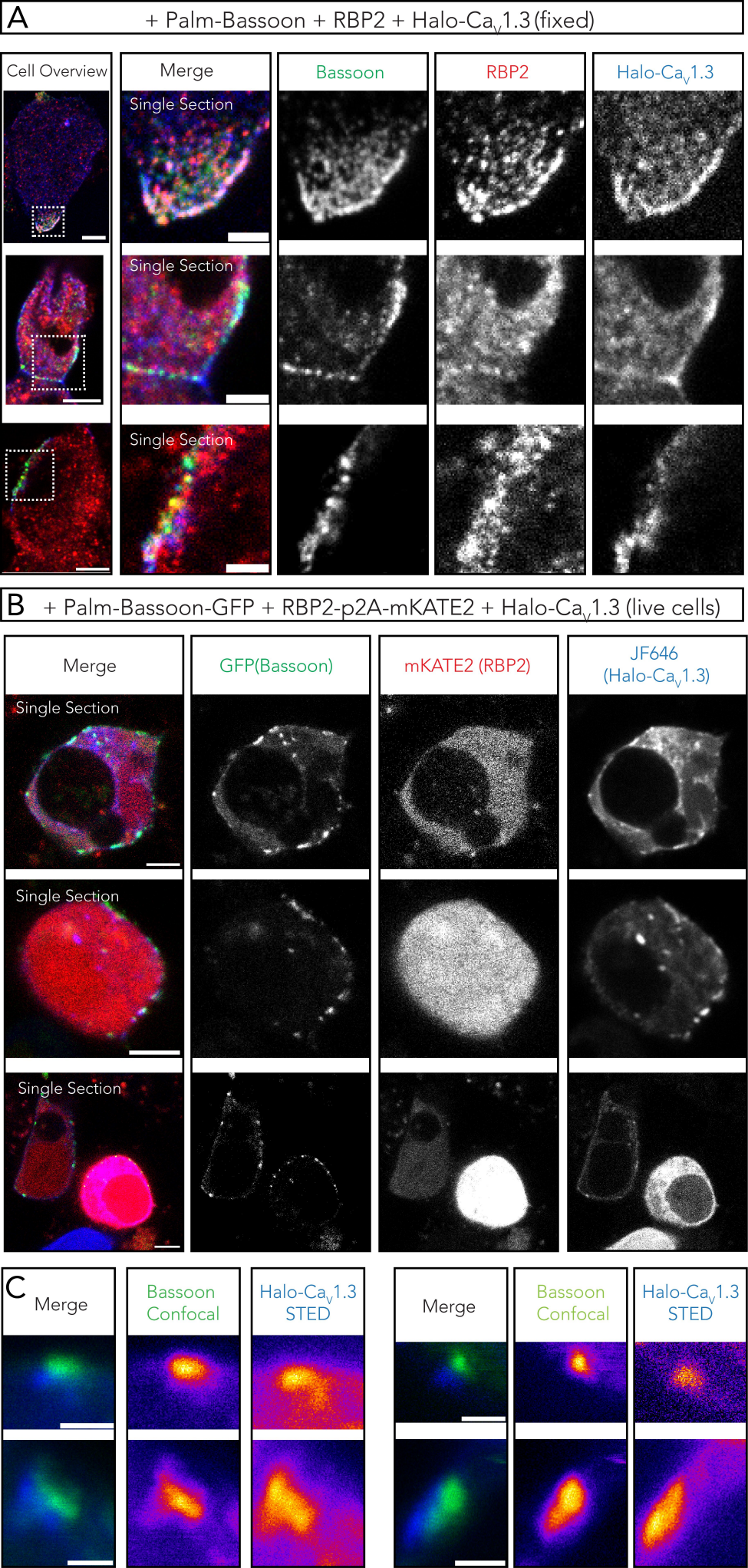
A
+ Palm-Bassoon + RBP2 + Halo-Ca$_V$1.3 (fixed)
Cell Overview
Merge
Bassoon
RBP2
Halo-Ca$_V$1.3
Single Section
Single Section
Single Section
B
+ Palm-Bassoon-GFP + RBP2-p2A-mKATE2 + Halo-Ca$_V$1.3 (live cells)
Merge
GFP(Bassoon)
mKATE2 (RBP2)
JF646 (Halo-Ca$_V$1.3)
Single Section
Single Section
Single Section
C
Merge
Bassoon Confocal
Halo-Ca$_V$1.3 STED
Merge
Bassoon Confocal
Halo-Ca$_V$1.3 STED

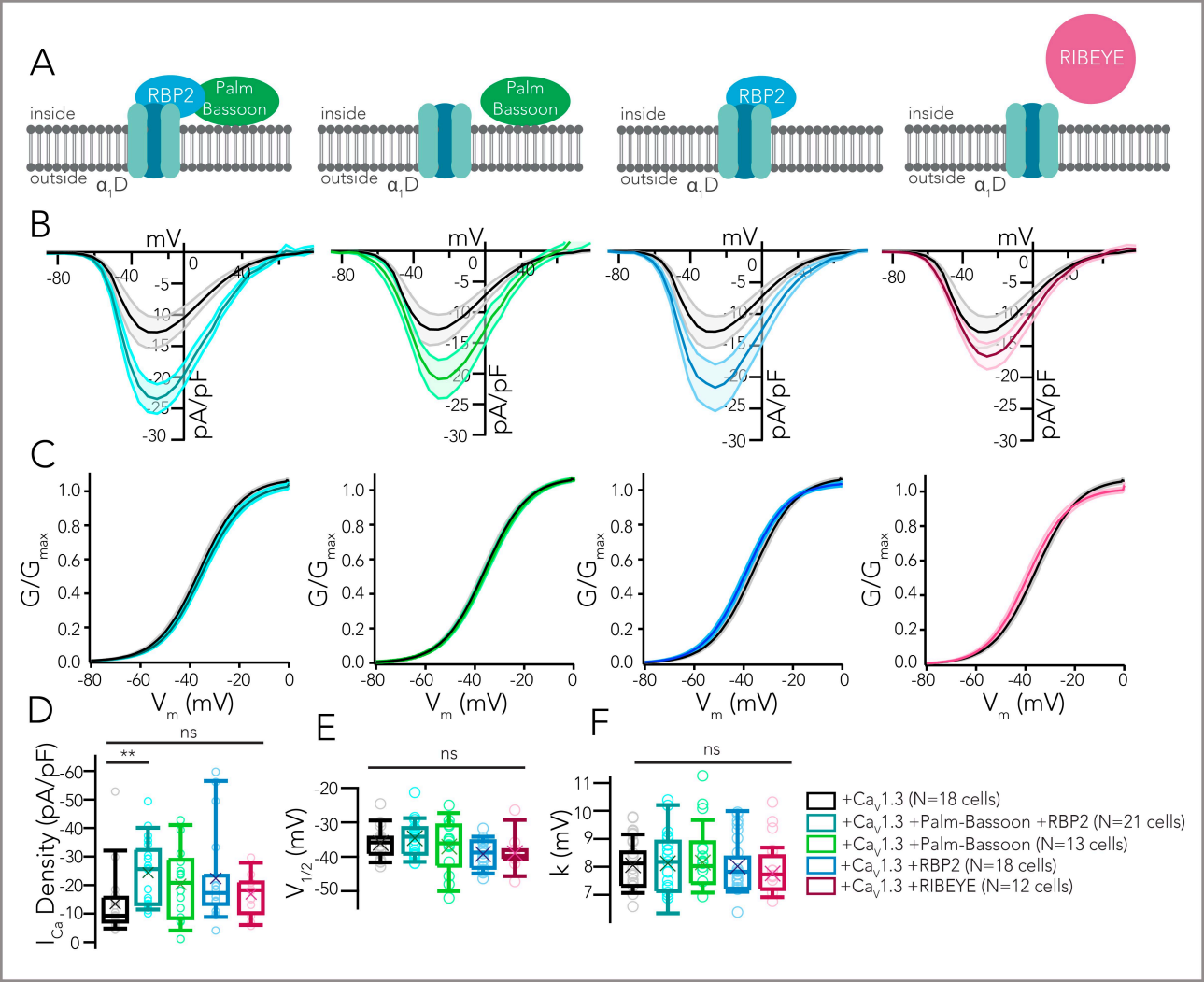
A
RBP2
Palm Bassoon
RIBEYE
inside
outside
α1D
B
mV
pA/pF
C
G/Gmax
Vm (mV)
D
ns
**
ICa Density (pA/pF)
E
V1/2 (mV)
F
k (mV)
+Cav1.3 (N=18 cells)
+Cav1.3 +Palm-Bassoon +RBP2 (N=21 cells)
+Cav1.3 +Palm-Bassoon (N=13 cells)
+Cav1.3 +RBP2 (N=18 cells)
+Cav1.3 +RIBEYE (N=12 cells)

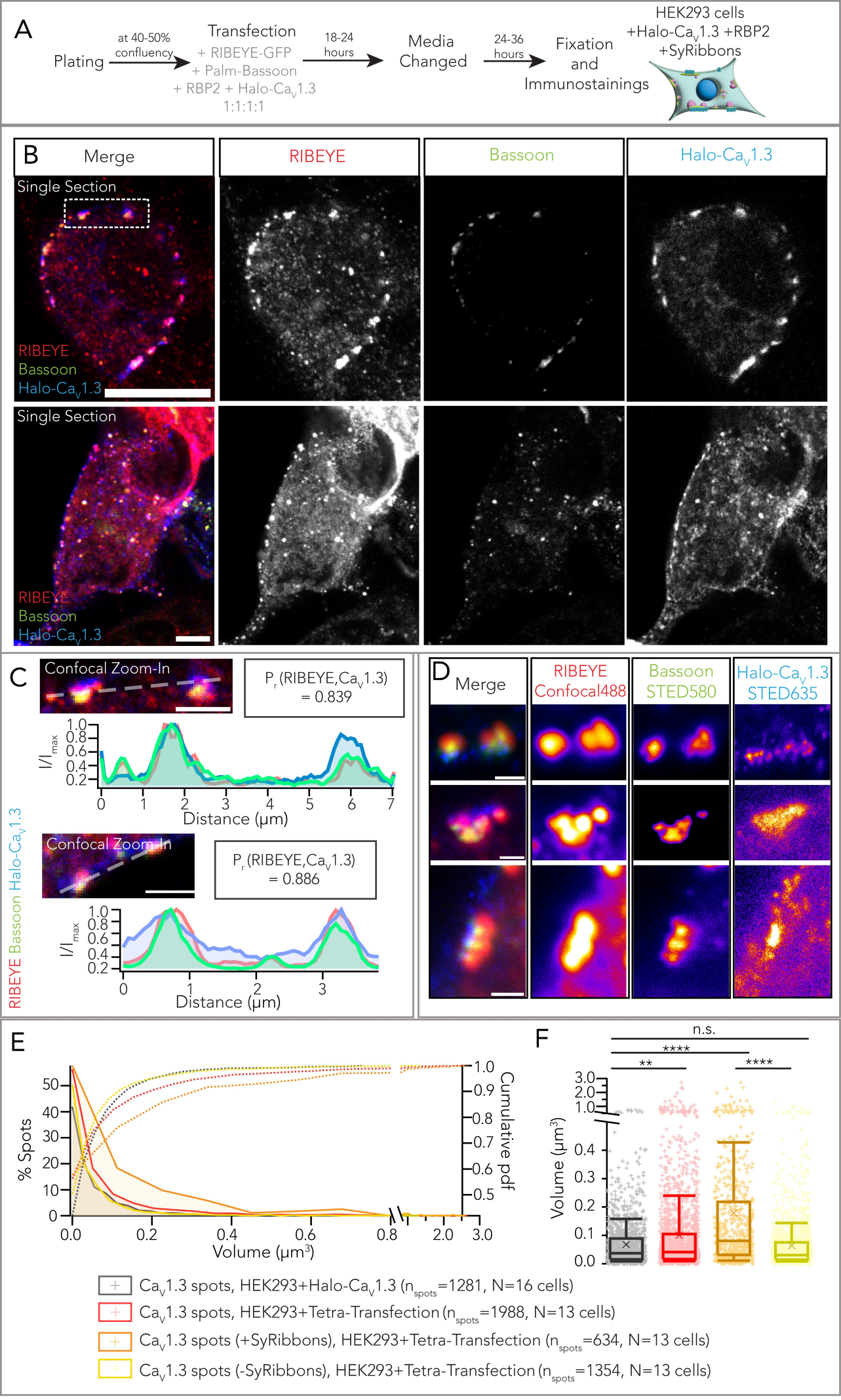
A
Plating
at 40-50% confluency
Transfection
+ RIBEYE-GFP
+ Palm-Bassoon
+ RBP2 + Halo-CaV1.3
1:1:1:1
18-24 hours
Media Changed
24-36 hours
Fixation and Immunostainings
HEK293 cells
+Halo-CaV1.3 +RBP2
+SyRibbons
B
Merge
RIBEYE
Bassoon
Halo-CaV1.3
Single Section
RIBEYE
Bassoon
Halo-CaV1.3
Single Section
RIBEYE
Bassoon
Halo-CaV1.3
C
Confocal Zoom-In
Pr(RIBEYE,CaV1.3) = 0.839
I/Imax
Distance (µm)
Confocal Zoom-In
Pr(RIBEYE,CaV1.3) = 0.886
I/Imax
Distance (µm)
RIBEYE Bassoon Halo-CaV1.3
D
Merge
RIBEYE Confocal488
Bassoon STED580
Halo-CaV1.3 STED635
E
% Spots
Cumulative pdf
Volume (µm³)
F
n.s.
****
**
****
Volume (µm³)
CaV1.3 spots, HEK293+Halo-CaV1.3 (nspots=1281, N=16 cells)
CaV1.3 spots, HEK293+Tetra-Transfection (nspots=1988, N=13 cells)
CaV1.3 spots (+SyRibbons), HEK293+Tetra-Transfection (nspots=634, N=13 cells)
CaV1.3 spots (-SyRibbons), HEK293+Tetra-Transfection (nspots=1354, N=13 cells)

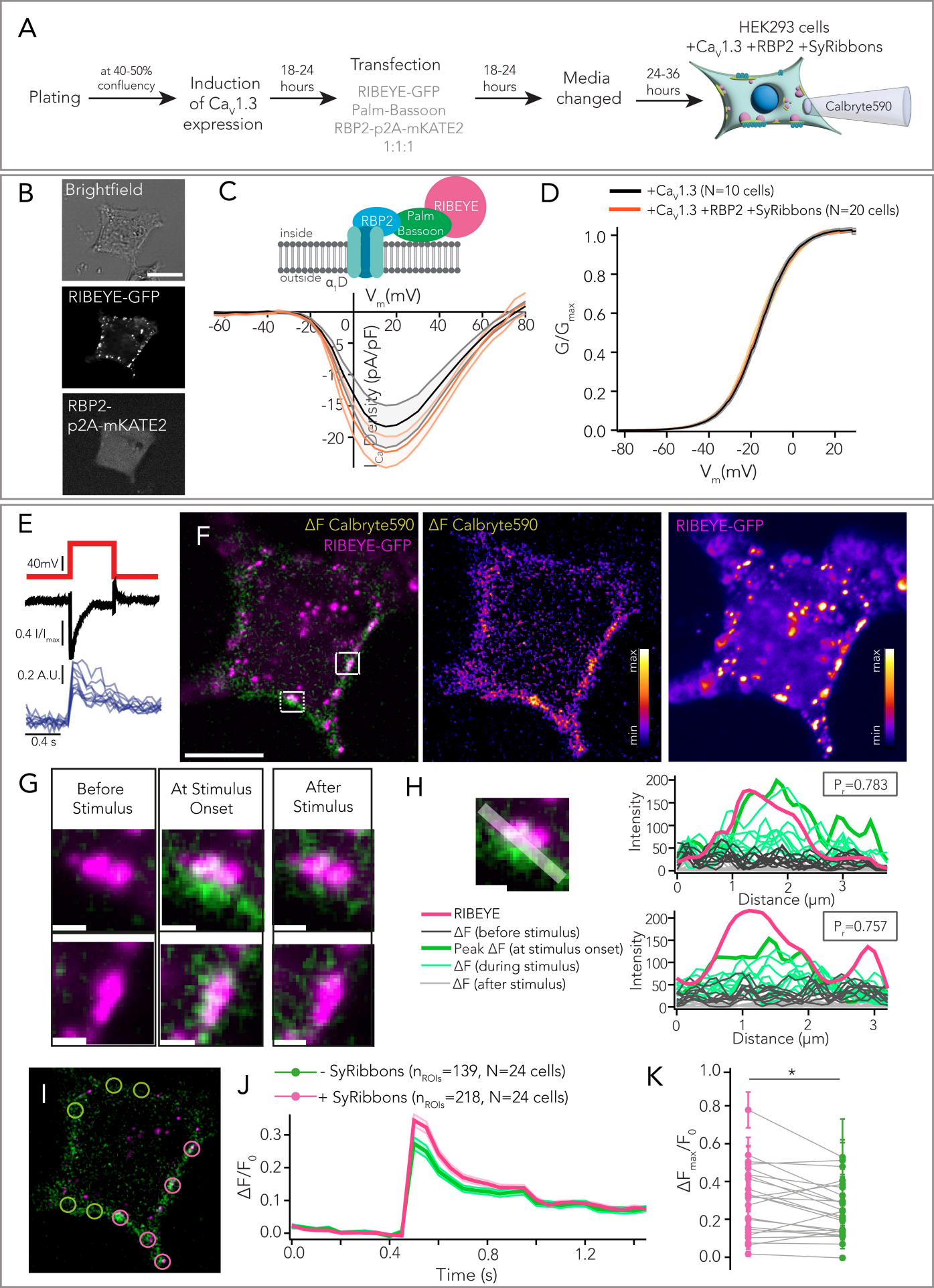
A
Plating
at 40-50% confluency
Induction of $Ca_V1.3$ expression
18-24 hours
Transfection
RIBEYE-GFP
Palm-Bassoon
RBP2-p2A-mKATE2
1:1:1
18-24 hours
Media changed
24-36 hours
HEK293 cells
$+Ca_V1.3$ +RBP2 +SyRibbons
Calbryte590
B
Brightfield
RIBEYE-GFP
RBP2-p2A-mKATE2
C
RIBEYE
RBP2
Palm Bassoon
inside
outside
α_1D
V_m(mV)
I_{Ca} Density (pA/pF)
D
$+Ca_V1.3$ (N=10 cells)
$+Ca_V1.3$ +RBP2 +SyRibbons (N=20 cells)
G/G_{max}
V_m(mV)
E
40mV
0.4 I/I_{max}
0.2 A.U.
0.4 s
F
ΔF Calbryte590
RIBEYE-GFP
ΔF Calbryte590
RIBEYE-GFP
max
min
G
Before Stimulus
At Stimulus Onset
After Stimulus
H
RIBEYE
ΔF (before stimulus)
Peak ΔF (at stimulus onset)
ΔF (during stimulus)
ΔF (after stimulus)
P_r=0.783
P_r=0.757
Intensity
Distance (μm)
I
J
- SyRibbons (n_{ROIs}=139, N=24 cells)
+ SyRibbons (n_{ROIs}=218, N=24 cells)
$\Delta F/F_0$
Time (s)
K
$\Delta F_{max}/F_0$
*

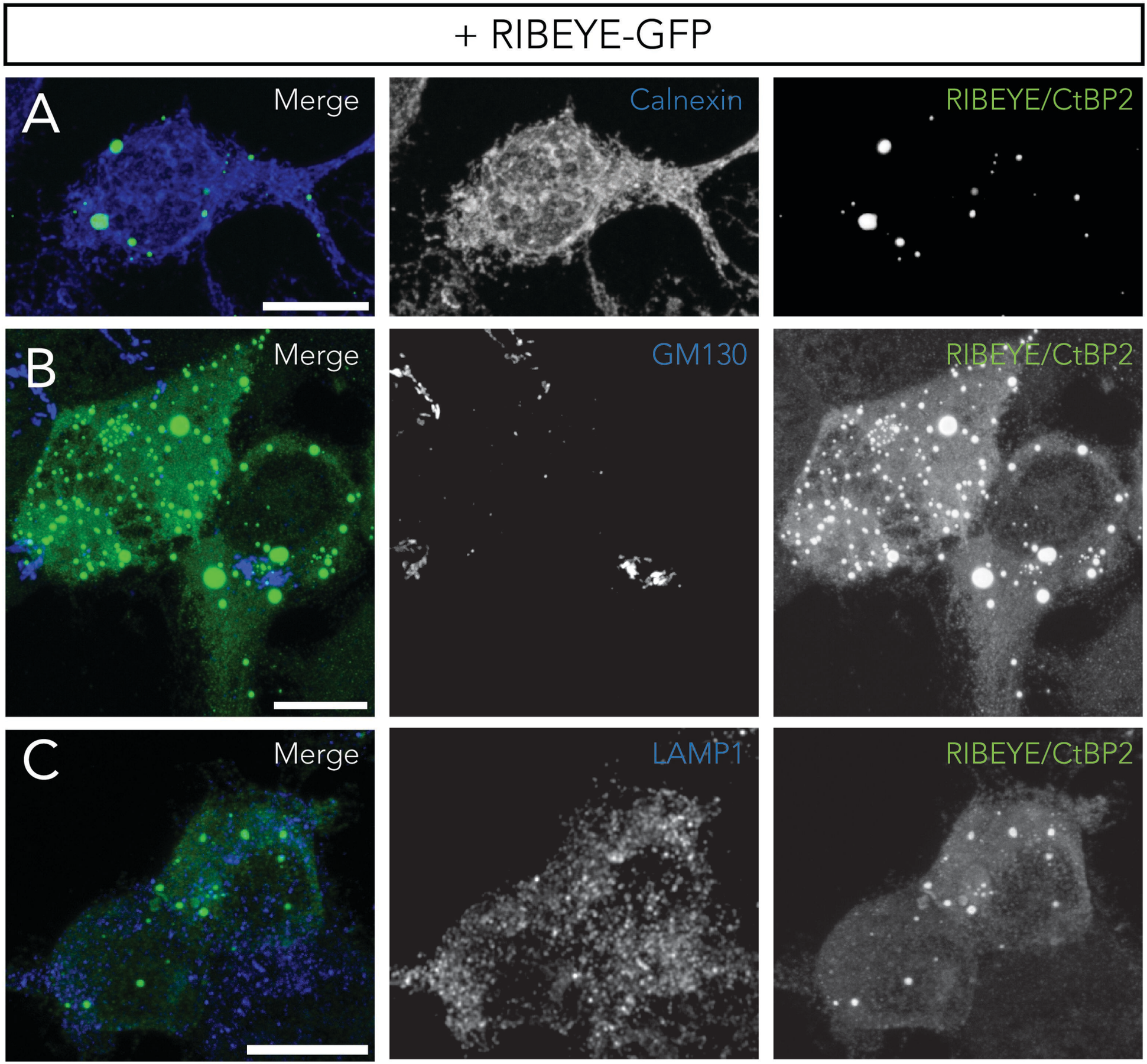
+ RIBEYE-GFP
A
Merge
Calnexin
RIBEYE/CtBP2
B
Merge
GM130
RIBEYE/CtBP2
C
Merge
LAMP1
RIBEYE/CtBP2

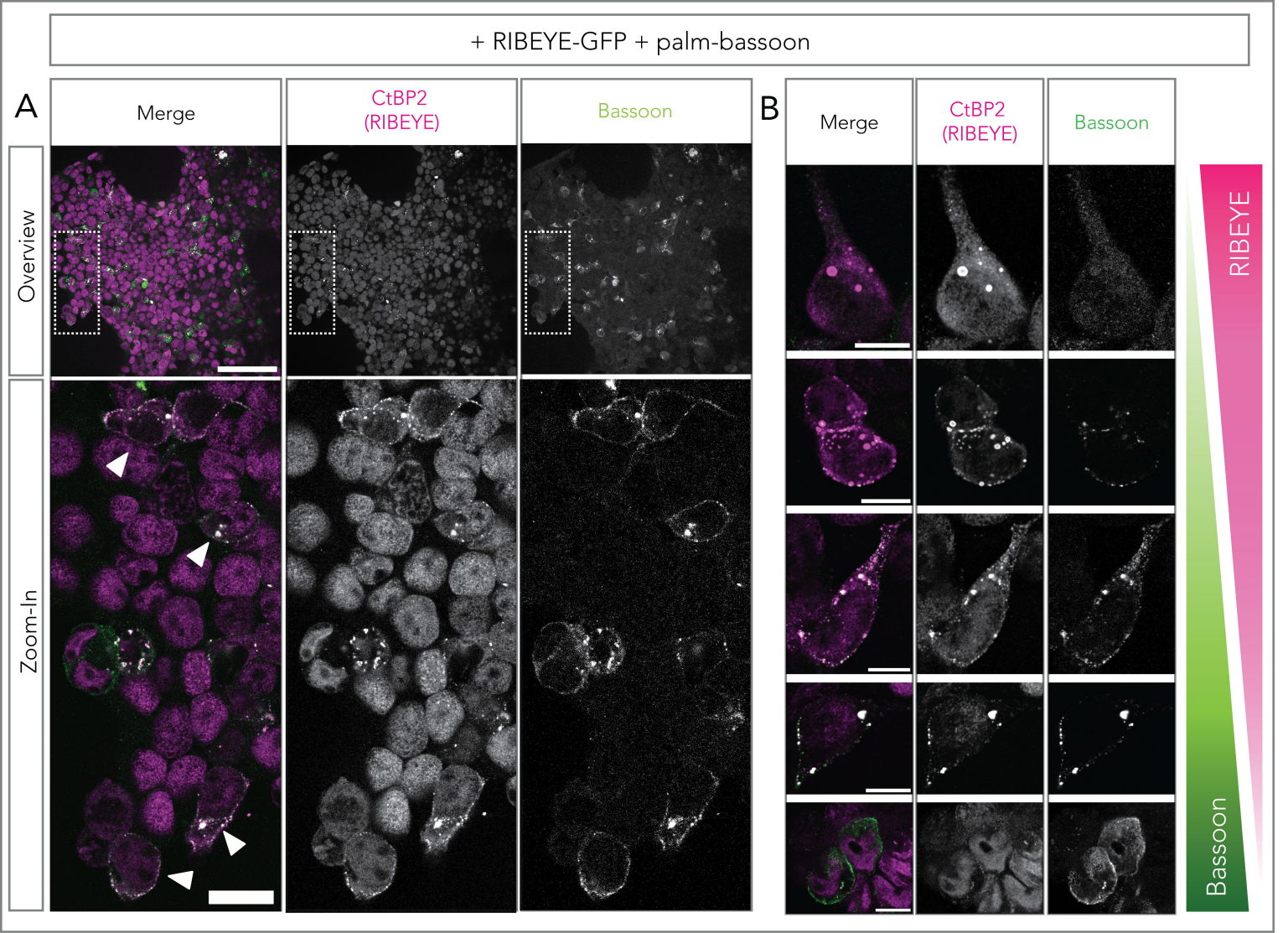
+ RIBEYE-GFP + palm-bassoon
A
Merge
CtBP2
(RIBEYE)
Bassoon
Overview
Zoom-In
B
Merge
CtBP2
(RIBEYE)
Bassoon
RIBEYE
Bassoon

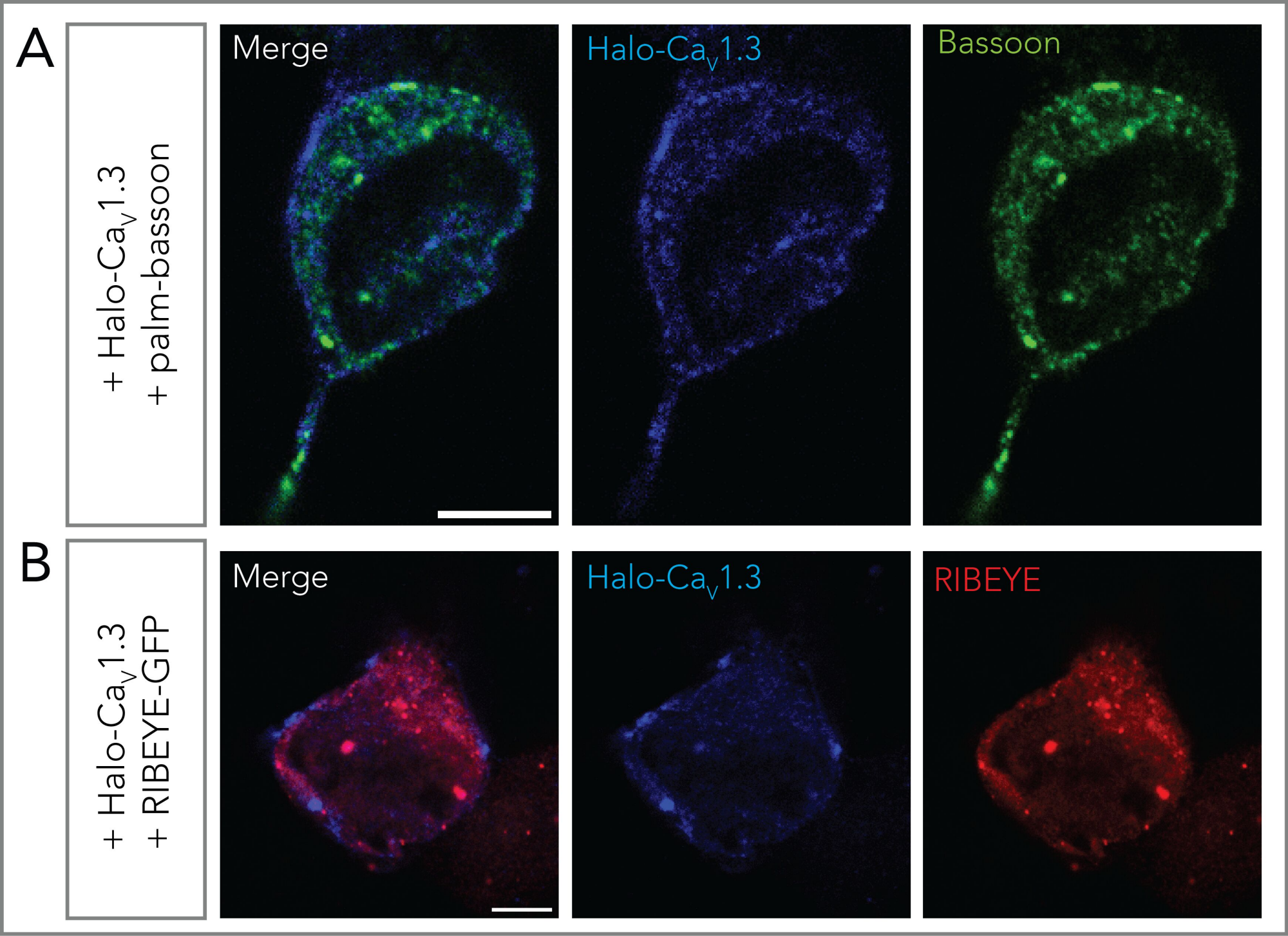
A
+ Halo-Ca$_V$1.3
+ palm-bassoon
Merge
Halo-Ca$_V$1.3
Bassoon
B
+ Halo-Ca$_V$1.3
+ RIBEYE-GFP
Merge
Halo-Ca$_V$1.3
RIBEYE

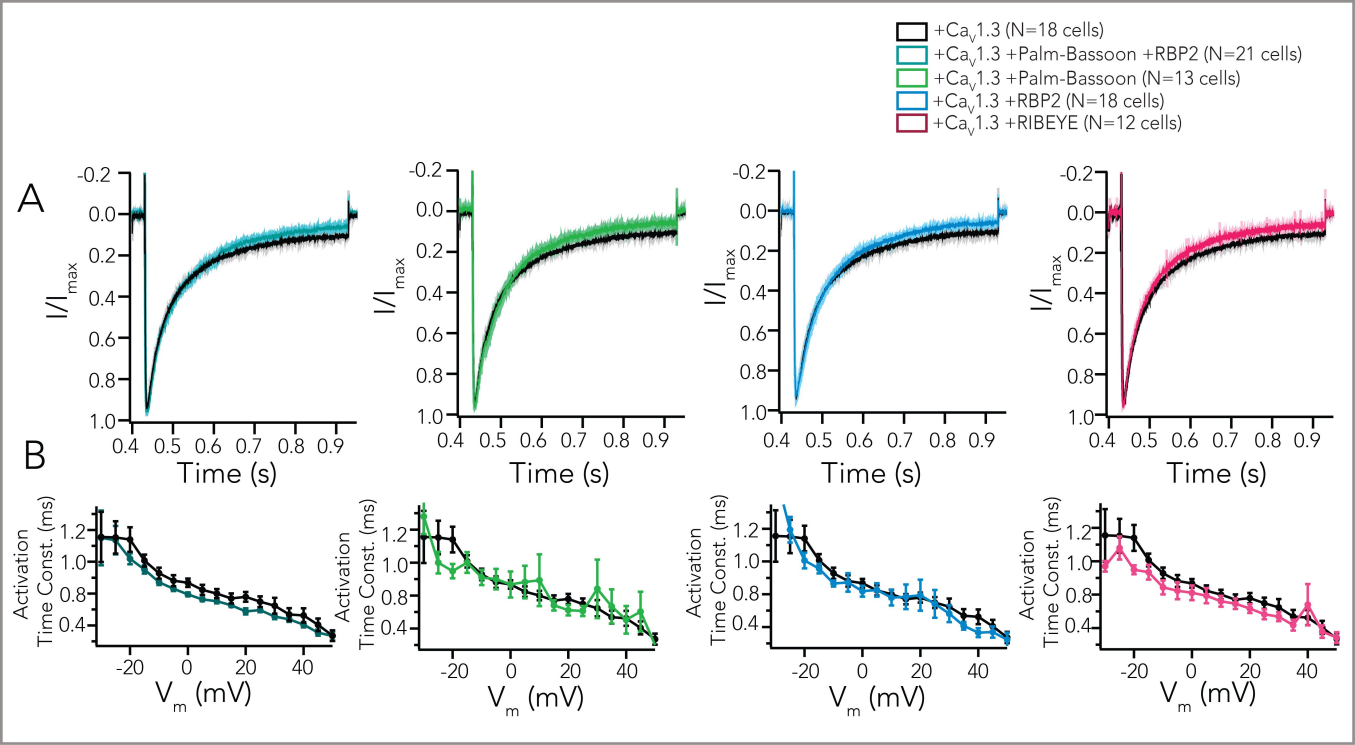
+Cav1.3 (N=18 cells)
+Cav1.3 +Palm-Bassoon +RBP2 (N=21 cells)
+Cav1.3 +Palm-Bassoon (N=13 cells)
+Cav1.3 +RBP2 (N=18 cells)
+Cav1.3 +RIBEYE (N=12 cells)
A
I/Imax
Time (s)
B
Activation Time Const. (ms)
Vm (mV)